





Article

# Determination of the Downwelling Diffuse Attenuation Coefficient of Lake Water with the Sentinel-3A OLCI

Ming Shen <sup>1,2</sup> , Hongtao Duan <sup>1,\*</sup> , Zhigang Cao <sup>1,2</sup> , Kun Xue <sup>1</sup>, Steven Loiselle <sup>3</sup>  and Herve Yesou <sup>4</sup>

<sup>1</sup> Key Laboratory of Watershed Geographic Sciences, Nanjing Institute of Geography and Limnology, Chinese Academy of Sciences, Nanjing 210008, China; shm9306@163.com (M.S.); zgcao@niglas.ac.cn (Z.C.); kxue@niglas.ac.cn (K.X.)

<sup>2</sup> University of Chinese Academy of Sciences, Beijing 100049, China

<sup>3</sup> Dipartimento di Biotecnologie, Chimica e Farmacia, University of Siena, CSGI, Via Aldo Moro 2, Siena 53100, Italy; loiselle@unisi.it

<sup>4</sup> ICube—SERTIT, Université de Strasbourg, Institut Telecom Physiques Strasbourg, Parc d'Innovation, 300, Bd Sébastien Brant, BP 10413, F-67412 Illkirch Graffenstaden, France; herve.yesou@unistra.fr

\* Correspondence: htduan@niglas.ac.cn or htduan@gmail.com; Tel.: +86-25-8688-2161

Received: 1 November 2017; Accepted: 29 November 2017; Published: 1 December 2017

**Abstract:** The Ocean and Land Color Imager (OLCI) on the Sentinel-3A satellite, which was launched by the European Space Agency in 2016, is a new-generation water color sensor with a spatial resolution of 300 m and 21 bands in the range of 400–1020 nm. The OLCI is important to the expansion of remote sensing monitoring of inland waters using water color satellite data. In this study, we developed a dual band ratio algorithm for the downwelling diffuse attenuation coefficient at 490 nm ( $K_d(490)$ ) for the waters of Lake Taihu, a large shallow lake in China, based on data measured during seven surveys conducted between 2008 and 2017 in combination with Sentinel-3A-OLCI data. The results show that: (1) Compared to the available  $K_d(490)$  estimation algorithms, the dual band ratio (681 nm/560 nm and 754 nm/560 nm) algorithm developed in this study had a higher estimation accuracy ( $N = 26$ , coefficient of determination ( $R^2$ ) = 0.81, root-mean-square error (RMSE) =  $0.99 \text{ m}^{-1}$  and mean absolute percentage error (MAPE) = 19.55%) and validation accuracy ( $N = 14$ ,  $R^2 = 0.83$ , RMSE =  $1.06 \text{ m}^{-1}$  and MAPE = 27.30%), making it more suitable for turbid inland waters; (2) A comparison of the OLCI  $K_d(490)$  product and a similar Moderate Resolution Imaging Spectroradiometer (MODIS) product reveals a high consistency between the OLCI and MODIS products in terms of the spatial distribution of  $K_d(490)$ . However, the OLCI product has a smoother spatial distribution and finer textural characteristics than the MODIS product and contains notably higher-quality data; (3) The  $K_d(490)$  values for Lake Taihu exhibit notable spatial and temporal variations.  $K_d(490)$  is higher in seasons with relatively high wind speeds and in open waters that are prone to wind- and wave-induced sediment resuspension. Finally, the Sentinel-3A-OLCI has a higher spatial resolution and is equipped with a relatively wide dynamic range of spectral bands suitable for inland waters. The Sentinel-3B satellite will be launched soon and, together with the Sentinel-3A satellite, will form a two-satellite network with the ability to make observations twice every three days. This satellite network will have a wider range of application and play an important role in the monitoring of inland waters with complex optical properties.

**Keywords:** diffuse attenuation coefficient; Sentinel-3A OLCI; Lake Taihu; remote sensing

## 1. Introduction

After entering water, sunlight is absorbed and scattered by constituents in the water, such as suspended particulate matter (SPM), phytoplankton, and colored dissolved organic matter (CDOM), and its downwelling irradiance attenuates nearly exponentially with increasing depth. The downwelling diffuse attenuation coefficient,  $K_d$ , is a main parameter that characterizes underwater light fields.  $K_d$  is an apparent optical property that is determined collectively by factors such as absorption and backscattering by each constituent in the water, the incident light field, and the water depth [1,2]. However, the effects of light fields are generally insignificant, and  $K_d$  is therefore mainly determined by the inherent optical properties (e.g., absorption and scattering) of the water. Thus,  $K_d$  is also often referred to as a “quasi-inherent optical property” [3]. In fact, the strength of a light field at a depth  $z$  is affected by the transfer of light radiation from the surface of the water to the depth  $z$ , rather than by only the attenuation of the light beam at the depth  $z$ . Therefore, the commonly used parameter  $K_d$  is the vertical mean value of a certain layer of water [4].  $K_d$  is a basic parameter that characterizes underwater light fields [5] and plays a vital role in studying water turbidity [6], sediment transport and resuspension [7,8], heat transfer within the upper water [9,10], the photosynthesis of phytoplankton [11,12], and the net primary productivity of natural waters [13,14].

Satellite-based remote sensing is a more effective and rapid method for acquiring  $K_d$  over large areas than conventional measurement methods. The  $K_d$  value at the wavelength of 490 nm ( $K_d(490)$ ) is one of the most commonly used standard water color remote sensing products [15]. Extensive research has been conducted to develop algorithms for estimating  $K_d$  for waters. Most of this research focuses on oceanic waters and can be classified into three types: (1) The type I research concerns the establishment of an empirical relationship between  $K_d$  and the chlorophyll *a* (Chl<sub>a</sub>) concentration [16] based on the observation that the optical properties of oceanic waters are mainly affected by phytoplankton; (2) The type II research focuses on the establishment of relationships between  $K_d(490)$  and the inherent optical properties and boundary conditions (e.g., the solar elevation angle and water surface conditions) of water using the radiative transfer theory-based semi-analytical algorithm [4,17–20]; (3) The type III research involves the establishment of statistical relationships between  $K_d(490)$  and the apparent optical properties (e.g., the water-leaving radiance,  $L_w$ , and remote sensing reflectance,  $R_{rs}$ ) [15,20–22]. The algorithms developed in these three types of research are mainly applicable to open oceanic waters and slightly turbid coastal waters.

Few studies have been conducted to estimate  $K_d(490)$  for inland lakes, particularly turbid shallow lakes, based on remote sensing data. Research has demonstrated that the  $K_d$  values for shallow lakes are one to two orders of magnitude greater than those for most oceanic or coastal waters [20,23,24]. The contributions of Chl<sub>a</sub>, suspended particulate inorganic matter (SPIM), and CDOM to light attenuation can vary significantly, both spatially and seasonally [25]. Relatively significant uncertainties are also associated with the atmospheric correction for these waters [26]. Therefore, algorithms commonly used for estimating  $K_d(490)$  for open oceanic waters and coastal waters cannot be used directly for highly turbid shallow lakes. The algorithms available for turbid inland waters are mostly empirical models. Shi et al. established a remote sensing-based single band algorithm for estimating the diffuse attenuation coefficient of the photosynthetically available radiation,  $K_d(\text{PAR})$ , for Lake Taihu using Medium Resolution Imaging Spectrometer (MERIS) top-of-atmosphere (TOA) radiance data in the 753-nm band [27]. Zheng et al. developed an algorithm for deriving  $K_d(490)$  for Dongting Lake from the ratio of Landsat data in the near-infrared (NIR) band to Landsat data in the red band [28]. Song et al. established a remote sensing-based algorithm for estimating  $K_d(\text{PAR})$  for lakes in Northeast China through a multiple stepwise regression analysis using Moderate Resolution Imaging Spectroradiometer (MODIS) and Landsat data [25]. These algorithms have significant spatial and seasonal limitations and differ significantly in satellite band selection. To our knowledge, no diffuse attenuation algorithm has been specifically developed for the Ocean and Land Color Imager (OLCI) sensor. Given the opportunities that this sensor presents, there is an urgent need to develop a simple, high-accuracy  $K_d(490)$  estimation algorithm that is suitable for turbid shallow lakes.

The OLCI sensor will be one of the main sensors for remote sensing-based monitoring of the color of inland waters for the next 15 years. The MERIS and MODIS sensors have been commonly used to monitor the water quality of turbid inland waters. However, the MERIS sensor stopped working in April 2012, and the MODIS sensor has been in operation for eight years longer than its planned service life and has started to suffer signal attenuation; consequently, it may soon stop operating. The OLCI, which is the optical payload on the Sentinel-3A satellite, part of the Copernicus Constellation, is a high-accuracy visible spectral imager [29]. As a sensor for observing ocean colors across the globe and the successor to the ENVISAT-MERIS, the OLCI is equipped with more spectral bands (21 bands in the range of 400–1020 nm) suitable for inland waters, especially full resolution (FR) data of 300 m, and has a higher stability (<https://earth.esa.int/web/sentinel/user-guides/sentinel-3-olci/resolutions/radiometric>). OLCI data have been used since October 2016. A satellite of the same type as the Sentinel-3A, the Sentinel-3B, is planned for launch in 2018. The Sentinel-3B and Sentinel-3A will form a two-satellite network that will be capable of performing observations once every 1.5 days, which compares favorably with the MODIS and thus has better prospects for highly variable inland waters.

This study examined the temporal and spatial distributions of  $K_d(490)$  in Lake Taihu, which is a large shallow lake in China, based on data measured during seven surveys conducted between 2008 and 2017 in combination with the Sentinel-3A-OLCI dataset from 2016–2017 to determine the characteristics of the photoecological environment in the waters of Lake Taihu. The main goals were: (1) to develop an algorithm for estimating  $K_d(490)$  for the waters of Lake Taihu based on OLCI sensor data and compare it with a MODIS product of the same type; and (2) to establish a long time-series  $K_d(490)$  dataset for Lake Taihu and determine the patterns of and driving factors for the temporal and spatial variations of  $K_d(490)$  in Lake Taihu. To our knowledge, this study is the first to investigate the temporal and spatial variations of  $K_d(490)$  in an inland lake using OLCI data. It is hoped that this study will significantly advance the application of OLCI data in research on inland lakes. The monitoring and application of long time-series data can be achieved with OLCI data in combination with ENVISAT-MERIS data.

## 2. Materials and Methods

### 2.1. Study Area

Lake Taihu ( $30^{\circ}56'–31^{\circ}34'N$ ,  $119^{\circ}54'–120^{\circ}36'E$ , Figure 1) is the third-largest freshwater lake in China. It is a large, shallow, and eutrophic lake located in the Yangtze River basin, and it has a surface area of 2338 km<sup>2</sup> and a mean depth of 1.9 m. Lake Taihu represents typical case II waters with complex optical properties and high spatial variability [30,31]. Lake Taihu is consistently turbid due to frequent wind-wave-induced resuspension, whereas the waters in East Lake Taihu are often clear with aquatic macrophytes [32,33]. In addition, Lake Taihu suffers from frequent algal blooms in the spring and summer, which severely impacts the normal life of the several million nearby residents [34,35].

### 2.2. Field Measurements

Seven field surveys were performed between 2008 and 2017 (October 2008, January 2011, May 2011, March 2013, November 2016, March 2017, and April 2017; Figure 1 and Table 1). The remote sensing reflectance ( $R_{rs}$ ) and the downwelling diffuse attenuation coefficient ( $K_d$ ) were measured in situ, and water samples were collected at the surface (~30 cm) with a standard two-liter polyethylene water-fetching instrument immediately after the optical radiometric measurements. The water samples were stored in the dark at a low temperature (4 °C) before the laboratory analyses of Chla (µg/L), SPM (mg/L), SPIM (mg/L), suspended particulate organic matter (SPOM, mg/L), and absorption coefficients (m<sup>-1</sup>). Environmental parameters, such as the surface wind speed and cloud conditions, were recorded simultaneously.

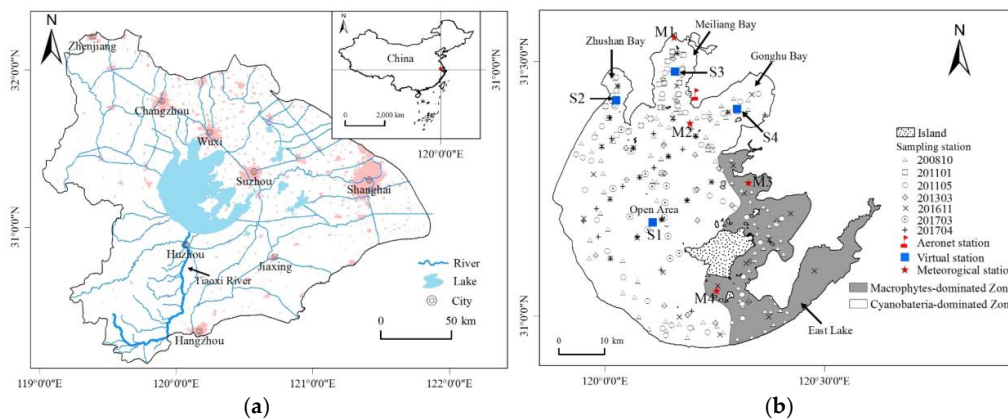


**Figure 1.** Location of Lake Taihu, China. (a) The Lake Taihu Basin is a flat region, and the Tiaoxi River (denoted by the black arrow) exhibits the maximum inflow; (b) following convention, the lake is divided into several segments. The black symbols with different shapes indicate sampling stations during seven cruise surveys in October 2008, January 2011, May 2011, March 2013, November 2016, March 2017, and April 2017. The red flag is the AERONET station, and the red stars are meteorological stations. The blue squares indicate four virtual stations located in different lake segments.

Laboratory analyses: Chla was measured spectrophotometrically. The water samples were first filtered using Whatman GF/C glass-fiber filters (pore size of 1.1  $\mu\text{m}$ ), and pigments were extracted with 90% acetone. The Chla concentrations were calculated from the absorbances at 630, 645, 663, and 750 nm, which were measured by a Shimadzu UV-2600 spectrophotometer [36]. The SPM concentrations were gravimetrically determined from samples collected on pre-combusted and pre-weighed 47 mm Whatman GF/C glass-fiber filters that were dried at 105  $^{\circ}\text{C}$  overnight. SPM was differentiated into SPIM and SPOM by burning organic matter from the filters at 550  $^{\circ}\text{C}$  for 3 h and weighing the filters again [36–38]. The absorption coefficients of the total particulate matter ( $a_p$ ), phytoplankton pigments ( $a_{ph}$ ), and detritus ( $a_d$ ) were determined using the quantitative filter technique [39,40] with 47 mm Whatman GF/C glass-fiber filters and a Shimadzu UV-2600 spectrophotometer. After measuring the total particulate absorption ( $a_p$ ), the absorption of the detrital particles ( $a_d$ ) was determined from the absorbance measured after the pigments were bleached with sodium hypochlorite, and the difference was the absorption of phytoplankton pigments ( $a_{ph}$ ). The CDOM absorption ( $a_g$ ) was determined from filtered water (Millipore filter with a 0.22  $\mu\text{m}$  pore size) using a Shimadzu UV-2600 spectrophotometer with Milli-Q water as the reference [41,42].

Remote sensing reflectance ( $R_{rs}$ ): Following NASA protocols [43], the downwelling radiance and upwelling total radiance above the water surface were measured with the above-water measurement method using ASD field spectrometers. A FieldSpec Pro Dual VINR spectroradiometer (350–1050 nm, Analytical Spectral Devices, Inc.) was used to measure the remote sensing reflectance before December 2016, and a FieldSpec Pro HandHeld 2 hand-held spectroradiometer (325–1075 nm, Analytical Spectral Devices, Inc.) was used after. The total water leaving radiance ( $L_{sw}$ ), radiance of the gray panel ( $L_p$ ), and sky radiance ( $L_{sky}$ ) were measured to obtain  $R_{rs}$ :

$$R_{rs}(\lambda) = (L_{sw}(\lambda) - r \cdot L_{sky}(\lambda)) / (L_p(\lambda) \cdot \pi / \rho_p(\lambda)) \quad (1)$$

where  $r$  is the air-water surface reflectance (a value of 2.5% was used), and  $\rho_p(\lambda)$  is the reflectance of the standard reflectance panel.

Downwelling diffuse attenuation coefficient ( $K_d$ ): The downwelling irradiance ( $E_d(\lambda, z)$ ) was measured using a TriOS RAMSES-ARC (Ramses, Germany) with a spectral resolution of 3.3 nm and a sampling interval of 1 nm. Measurements were made from the sunny side of the boat. The downwelling diffuse attenuation coefficient ( $K_d$ ) was determined as the slope of a least-squares regression fit to the measured  $\ln(E_d)$  as a function of depth ( $z$ ), as shown in the following formula [4,5,18]:



$$K_d(\lambda) = -\frac{1}{z} \ln \frac{E_d(\lambda, z)}{E_d(\lambda, 0^-)} \quad (2)$$

where  $E_d(\lambda, 0^-)$  and  $E_d(\lambda, z)$  are the downwelling irradiances immediately beneath the water surface and at depth  $z$ , respectively. Only the  $K_d(\lambda)$  values from regression fits of  $R^2 \geq 0.95$  were accepted [44]. Four to six depths were used in the regressions depending on the penetration depth. Note that before December 2016, measurements were made every 0.30 m down to the lake bottom, usually at five depths (0.30, 0.60, 0.90, 1.20, and 1.50 m); after December 2016, a WH3111 liquid level transmitter (Shenzhen Oriental Vanward Instrument Co., Ltd., Shenzhen, China) was installed on the TriOS underwater spectroradiometer to obtain more accurate downwelling irradiance profile data (with an interval of  $\sim 0.02$  m and usually more than 50 profiles). Significant correlations between the in situ measured  $K_d(490)$  obtained using the two measurement schemes were observed ( $r = 0.98$ ,  $p < 0.001$ ).

### 2.3. Satellite Image Acquisition and Pre-Processing

Twenty four scenes of Sentinel-3A-OLCI Level-1B data over Lake Taihu from November 2016 to April 2017 with minimal or no cloud cover were chosen and downloaded from the European Space Agency Copernicus Open Access Hub (previously known as the Sentinels Scientific Data Hub; <https://scihub.copernicus.eu/>). The OLCI Level-1B products include top-of-atmosphere (TOA) radiances for the 21 OLCI spectral bands, geolocation information, meteorological variables (e.g., total column water vapor and total columnar ozone), geographical information, and angles. Terra-MODIS Level-1A images captured on the same date as the OLCI data were downloaded from the NASA Ocean Color website (<http://oceancolor.gsfc.nasa.gov/>). Terra-MODIS data were used to take advantage of its near identical transit time over the study area, with respect to Aqua-MODIS, despite its lower-quality (e.g., radiometric quality and striping noise). Terra-MODIS Level-1A data were processed using SeaDAS 7.3 to generate Level-1B data. The satellite Level-1B data were processed in several steps (Figure 2).

**Atmospheric correction:** The Sentinel-3A OLCI Level 2 data are not used in this study since there are only  $R_{rs}$  products released in July 2017 and beyond. Also, the  $R_{rs}$  obtained by the SNAP C2RCC processor, when originally made available, did not provide a sufficiently high accuracy in Lake Taihu and was therefore not used. Instead, the Second Simulation of the Satellite Signal in the Solar Spectrum correction scheme (6S model) [45] was used to obtain  $R_{rs}$  from the Sentinel-3A-OLCI data over Lake Taihu. Many previous studies have shown that the results of the 6S model are more accurate and efficient than those of other calibration models over extremely turbid water [46,47]. The mid-latitude atmosphere model and continental aerosol model were adopted. The aerosol optical depth (AOD) data measured at the Taihu site using a CE318 Sunphotometer were obtained from AERONET (AERosol RObotic NETwork, <https://aeronet.gsfc.nasa.gov/>). The AERONET data include the AOD at 340, 380, 440, 500, 675, 870, 1020, and 1640 nm, the Ångström exponent, and the columnar water vapor. The AOD at 550 nm (required as an input to the 6S model) was calculated from the measured AOD and Ångström exponent.

**Cloud and algal blooms mask:** Due to thick aerosols and floating algae, the application of several existing cloud detection algorithms did not lead to acceptable results [34,48,49]. Thus, regions with clouds were manually outlined and masked. The floating algae index (FAI) [48] was calculated first, and the algae pixel-growing algorithm (APA) [50] was used to obtain the algal bloom coverage, which was used to mask the algal bloom areas.

**Satellite-in situ comparison:** To maximize the number of possible matching pairs between the in situ and satellite observations without compromising quality, the acceptable time interval was relaxed to 6 h instead of the commonly used 3 h time interval. A spatial homogeneity test was then applied to the satellite data [51]; the test required half of the pixels in the  $3 \times 3$  window centered around the in situ stations to have valid data, and the variance limit for these valid pixels was  $< 10\%$ . Note that there are a total of 40 matchups obtained in November 2016, March 2017, and April 2017 according to the strict criteria.

**Table 1.** Water parameters and optical properties of Lake Taihu, China. Chla, SPM, SPOM, and SPIM are chlorophyll a, suspended particle matter, suspended particulate organic matter, and suspended particulate inorganic matter, respectively. SDD is the Secchi disk depth, and  $a_d(440)$ ,  $a_g(440)$ , and  $a_{ph}(665)$  are the absorption coefficients of non-algal particulates, colored dissolved organic matter (CDOM), and phytoplankton, respectively.  $K_d(490)$  is the downwelling diffuse attenuation coefficient at 490 nm. S.D. is the standard deviation.

Parameters	Statistics	October-2008	Jane-2011	May-2011	March-2013	November-2016	March-2017	April-2017
Chla ( $\mu\text{g/L}$ )	Range	0.46–148.30	10.80–31.00	1.75–46.70	6.57–51.26	5.60–105.26	17.79–88	9.85–157.05
	Mean $\pm$ S.D.	21.89 $\pm$ 20.50	17.68 $\pm$ 7.27	14.35 $\pm$ 10.80	20.77 $\pm$ 12.90	24.94 $\pm$ 22.99	32.79 $\pm$ 21.17	46.32 $\pm$ 31.84
SPM (mg/L)	Range	1.57–94.80	9.40–44.45	10.92–150.60	5.00–127.00	22.00–125.00	24.00–180.00	21.33–130.67
	Mean $\pm$ S.D.	33.75 $\pm$ 18.34	22.53 $\pm$ 8.59	44.67 $\pm$ 28.58	61.39 $\pm$ 36.02	51.21 $\pm$ 26.41	113.33 $\pm$ 48.87	49.52 $\pm$ 24.07
SPOM (mg/L)	Range	1.00–29.27	4.90–26.25	3.52–41.13	1.00–41.00	6.00–81.00	9.33–22.67	9.33–64.00
	Mean $\pm$ S.D.	10.67 $\pm$ 4.60	7.62 $\pm$ 4.94	7.95 $\pm$ 5.74	13.98 $\pm$ 10.67	15.45 $\pm$ 13.22	18.31 $\pm$ 3.79	23.68 $\pm$ 12.85
SPIM (mg/L)	Range	0.57–71.10	4.20–24.80	6.92–132.45	0.50–116.00	12.00–85.00	13.33–157.33	6.67–69.33
	Mean $\pm$ S.D.	23.07 $\pm$ 14.87	14.91 $\pm$ 6.37	36.72 $\pm$ 25.60	47.41 $\pm$ 31.81	35.76 $\pm$ 20.40	95.02 $\pm$ 46.14	25.83 $\pm$ 15.63
$a_d(440)$ ( $\text{m}^{-1}$ )	Range	0.16–6.06	0.36–1.71	0.11–2.68	0.48–6.55	0.65–4.58	0.72–8.00	0.17–3.54
	Mean $\pm$ S.D.	2.01 $\pm$ 1.14	1.00 $\pm$ 0.43	0.86 $\pm$ 0.58	2.30 $\pm$ 1.34	2.10 $\pm$ 0.87	4.14 $\pm$ 2.07	1.37 $\pm$ 0.86
$a_g(440)$ ( $\text{m}^{-1}$ )	Range	0.40–1.67	0.57–2.42	0.40–4.16	0.34–0.97	0.30–5.15	0.49–1.60	0.56–2.29
	Mean $\pm$ S.D.	0.87 $\pm$ 0.28	1.35 $\pm$ 0.62	1.37 $\pm$ 0.98	0.62 $\pm$ 0.14	1.55 $\pm$ 0.83	0.85 $\pm$ 0.29	1.19 $\pm$ 0.60
$a_{ph}(665)$ ( $\text{m}^{-1}$ )	Range	0.01–0.85	0.26–0.88	0.05–0.94	0.20–1.12	0.05–0.92	0.20–0.98	0.16–2.42
	Mean $\pm$ S.D.	0.18 $\pm$ 0.15	0.43 $\pm$ 0.18	0.31 $\pm$ 0.20	0.41 $\pm$ 0.22	0.29 $\pm$ 0.18	0.44 $\pm$ 0.21	0.67 $\pm$ 0.47
$K_d(490)$ ( $\text{m}^{-1}$ )	Range	0.73–7.59	1.58–4.85	2.58–7.14	2.24–8.04	2.71–10.68	/	1.84–8.40
	Mean $\pm$ S.D.	4.50 $\pm$ 1.88	3.23 $\pm$ 1.09	4.52 $\pm$ 1.30	4.51 $\pm$ 1.52	5.71 $\pm$ 2.56	/	4.01 $\pm$ 1.92

Note: / indicates no measurement.

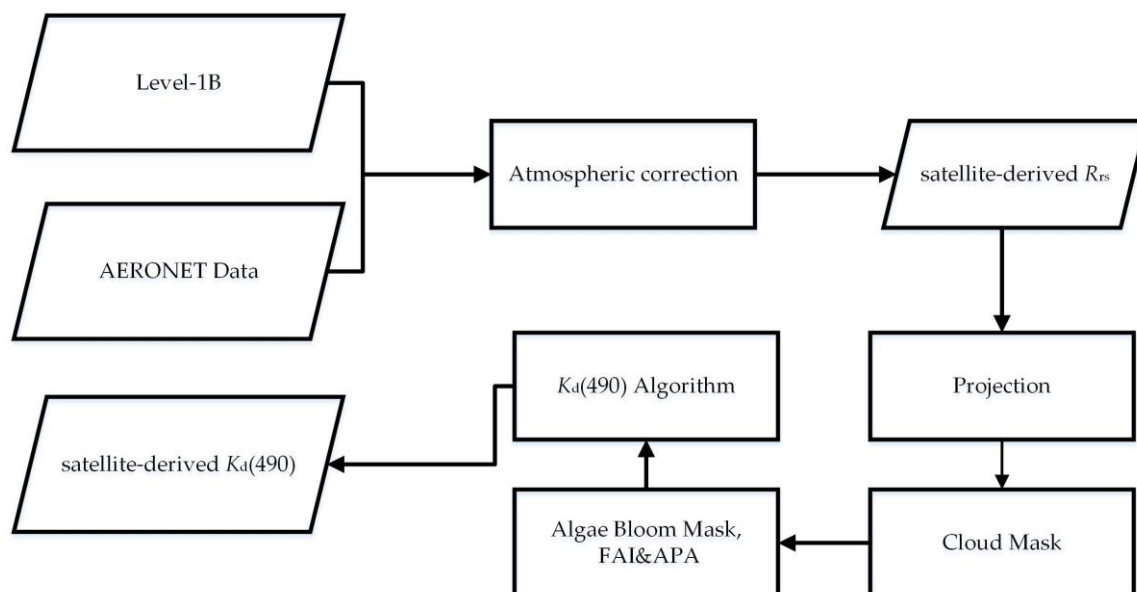


Figure 2. Processing procedure of the satellite-derived  $K_d(490)$  product.

#### 2.4. Meteorological Data

Meteorological data measured at the Jiangyin, Wuxi, Suzhou, and Dongshan meteorological stations near Lake Taihu (Figure 1), including precipitation and wind speed data, were obtained from the China Meteorological Data Sharing Service System (<http://data.cma.cn/>). Significant correlations between the meteorological data from the four meteorological stations were observed (hourly wind speed:  $r > 0.59$ ,  $p < 0.01$ ; daily precipitation:  $r > 0.85$ ,  $p < 0.01$ ). Thus, to analyze the variation of  $K_d(490)$ , we used the mean hourly wind speed and daily precipitation of the four stations to characterize the meteorological data for the entire lake.

#### 2.5. Statistical Analysis and Accuracy Assessment

The algorithm's performance was assessed using four indices based on the absolute error ( $\alpha = Y_i - X_i$ ) and the relative error ( $\beta = (Y_i - X_i)/X_i$ ), namely, the root mean square error (RMSE = root mean square of  $\alpha$ ), relative root mean square error (RMSE<sub>rel</sub> = root mean square of  $\beta$ ), mean normalized bias (MNB = arithmetic mean of  $\beta$ ), and normalized root mean square error (NRMS = standard deviation of  $\beta$ ) [42].  $X_i$  and  $Y_i$  refer to the measured and predicted values for the  $i$ th sample, respectively. Note that MNB is a measure of the systematic errors, whereas NRMS is a measure of the random errors.

### 3. Results

#### 3.1. Biogeochemical and Optical Characterization

The data measured during the seven surveys conducted between 2008 and 2017 show that each main color parameter of the waters of Lake Taihu varied over a wide range (Table 1). The Chl<sub>a</sub> concentration ranged from 0.46 to 157.05  $\mu\text{g/L}$  with a mean value of  $33.90 \pm 63.78 \mu\text{g/L}$ , and the total SPM concentration ranged from 1.57 to 180.00  $\text{mg/L}$  with a mean value of  $45.15 \pm 36.05 \text{mg/L}$ . The  $a_g(440)$  values of CDOM at the wavelength of 440 nm ranged from 0.40 to 2.42  $\text{m}^{-1}$  with a mean value of  $0.98 \pm 0.46 \text{m}^{-1}$ . The mean SPIM concentration was  $29.04 \pm 22.55 \text{mg/L}$ , and the mean SPOM concentration was  $10.16 \pm 6.31 \text{mg/L}$ . The Pearson correlation coefficient between the SPIM concentration and the total SPM concentration was as high as 0.87 ( $p < 0.001$ ), and SPIM accounted for more than 60% of the total SPM at 71% of the sampling sites, which indicates that SPIM is the dominant suspended matter in the waters of Lake Taihu. This finding agrees with a previous report [27]. Note that the samples with algal blooms and errors were not included in this analysis.

The magnitude of  $K_d$  is mainly influenced by changes in the absorption of dissolved matter, together with the absorption and scattering of particulate matter, over a background  $K_d$  related to pure water [52]. An analysis of the correlations between  $K_d(490)$  and the main color parameters (Figure 3) shows significant statistical correlations between  $K_d(490)$  and all of the main color parameters ( $p < 0.001$ ) except for CDOM's  $a_g(440)$  ( $p > 0.1$ ). It is worth noting that the correlation coefficient between  $K_d(490)$  and the SPIM concentration ( $r = 0.88$ ) is significantly higher than that between  $K_d(490)$  and the SPOM concentration ( $r = 0.22$ ) and that between  $K_d(490)$  and the Chla concentration ( $r = 0.15$ ). There is also a significant correlation coefficient between  $K_d(490)$  and the total SPM concentration ( $r = 0.88$ ,  $p < 0.001$ ) as SPIM is the dominant suspended matter in the waters of Lake Taihu. This suggests that in the absence of algal blooms,  $K_d(490)$  for the waters of Lake Taihu is mainly controlled by SPIM, followed by SPOM and phytoplankton pigments, and is insignificantly affected by CDOM.

Overall, the waters of Lake Taihu are characterized by high SPM and Chla concentrations, and SPIM is the dominant component of SPM. In addition,  $K_d(490)$  for the waters of Lake Taihu is mainly controlled by SPIM, followed by SPOM and phytoplankton pigments, and is insignificantly affected by CDOM.

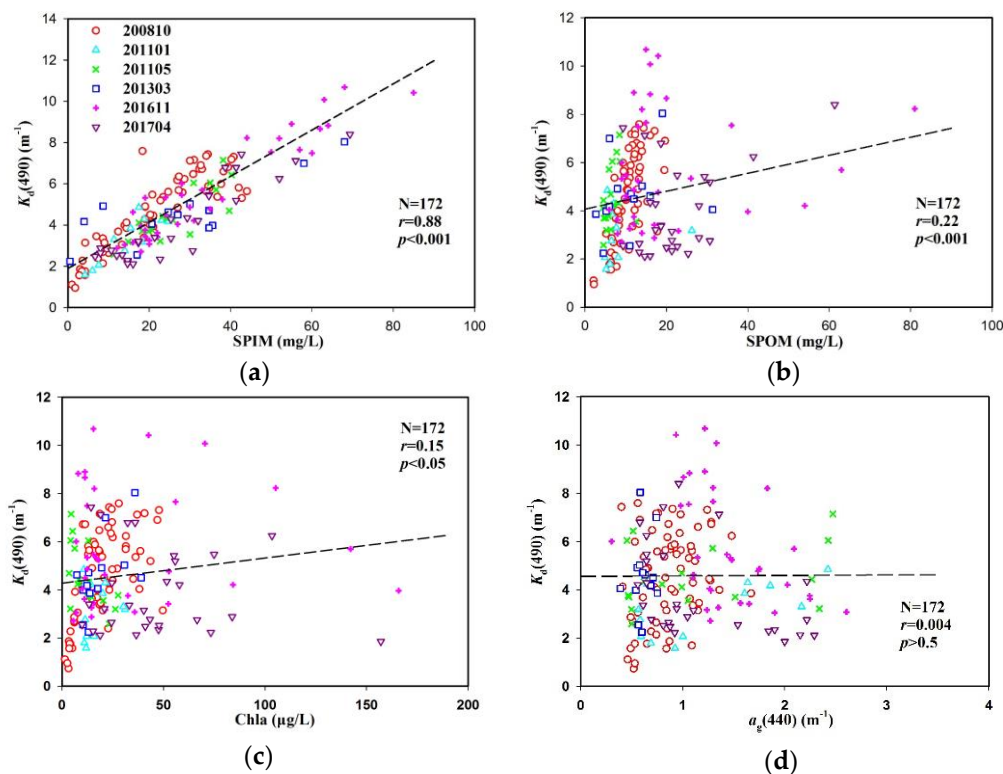


**Figure 3.** Relationships between  $K_d(490)$  and the bio-optical parameters of the water: (a) SPIM; (b) SPOM; (c) Chla; (d)  $a_g(440)$ .

### 3.2. Atmospheric Correction Assessment

Satellite-in situ matchups of 40 stations were used to evaluate the accuracy of the 6S atmospheric correction and then to develop and validate the satellite retrieval algorithm. By comparing the in situ measured  $R_{rs}$  and the OLCI-derived  $R_{rs}$  (Figure 4a), the 6S atmospheric correction model is found to perform well on the Sentinel-3A-OLCI data (RMSE  $< 0.0100 \text{ sr}^{-1}$ , MNB  $> -15.00\%$  and NRMS  $< 50.00\%$ ). Whereas the values obtained after the correction are generally lower than the actual measurements (MNB  $< 0$ ), the systematic and random errors are both within acceptable ranges. In particular, the accuracy is high in the 681-nm and 754-nm bands (RMSE  $< 0.0060 \text{ sr}^{-1}$ , MNB  $> -15.00\%$  and NRMS  $< 35.00\%$ ), which are the main bands used by the  $K_d$  algorithm.



The spectral shape of the OLCI-derived  $R_{rs}$  is generally consistent with that of the in situ measured  $R_{rs}$  (Figure 4b). Overall, the 6S model-based atmospheric correction method is able to acquire relatively high-accuracy  $R_{rs}$  data from OLCI data and can be further employed to estimate such water parameters as  $K_d(490)$  and the Chla and SPM concentrations based on remote sensing data.

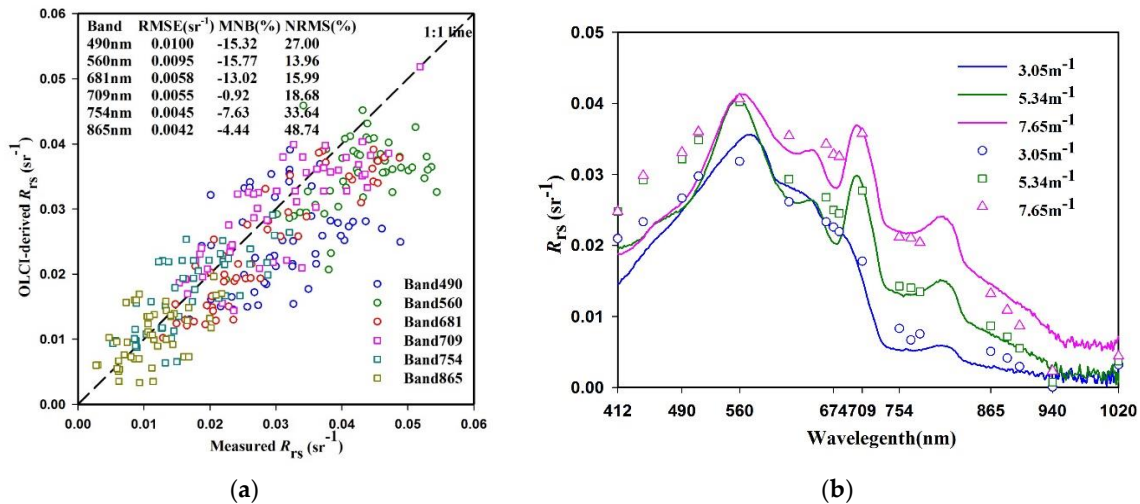


**Figure 4.** (a) Comparison of the  $R_{rs}$  measured in situ and the OLCI-derived  $R_{rs}$  after the 6S atmospheric correction for 40 matchups obtained in November 2016, March 2017, and April 2017; (b) comparison of the  $R_{rs}$  spectrum measured in situ and the OLCI-derived  $R_{rs}$  spectrum after the 6S atmospheric correction for different  $K_d(490)$  values. The lines represent the  $R_{rs}$  spectra from the in situ measurements, and the marks represent the OLCI-derived  $R_{rs}$  spectra after the 6S atmospheric corrections.

### 3.3. Development and Validation of the $K_d(490)$ Algorithm

The simultaneous sampling sites for  $K_d(490)$  were divided into two groups. Two thirds of the sampling sites ( $N = 26$ ) were used to establish an algorithm. To determine the optimal band or combination of bands for deriving  $K_d(490)$ , a correlation analysis was performed on the in situ measured  $K_d(490)$  and different OLCI-derived  $R_{rs}$  bands or combinations of OLCI-derived  $R_{rs}$  bands. The dual band ratio (681 nm/560 nm and 754 nm/560 nm) algorithm is found to have a high accuracy in estimating  $K_d(490)$  (Figure 5;  $R^2 = 0.81$ ,  $RMSE = 0.99 \text{ m}^{-1}$ ,  $RMSE_{rel} = 25.36\%$ ,  $MNB = 2.81\%$  and  $NRMS = 25.73\%$ ). The remote sensing-based algorithm for deriving  $K_d(490)$  from the OLCI-derived  $R_{rs}$  is as follows:

$$K_d(490) = 11.89 * \frac{R_{rs}(681)}{R_{rs}(560)} + 6.81 * \frac{R_{rs}(754)}{R_{rs}(560)} - 6.17 \quad (3)$$

The remaining one third of the data ( $N = 14$ ) was used to validate the algorithm (Figure 5). The validation accuracy of the algorithm is also high ( $R^2 = 0.83$ ,  $RMSE = 1.06 \text{ m}^{-1}$ ,  $RMSE_{rel} = 30.81\%$ ,  $MNB = -3.89\%$  and  $NRMS = 31.63\%$ ), and the intersection points between the measured and estimated values of  $K_d(490)$  are evenly distributed on both sides of the 1:1 line. This suggests that the algorithm has a high estimation accuracy for both high and low ranges and exhibits high consistency. Therefore, the dual band ratio algorithm generally has a high accuracy and applicability and can be used to derive  $K_d(490)$  for the waters of Lake Taihu from remote sensing data.

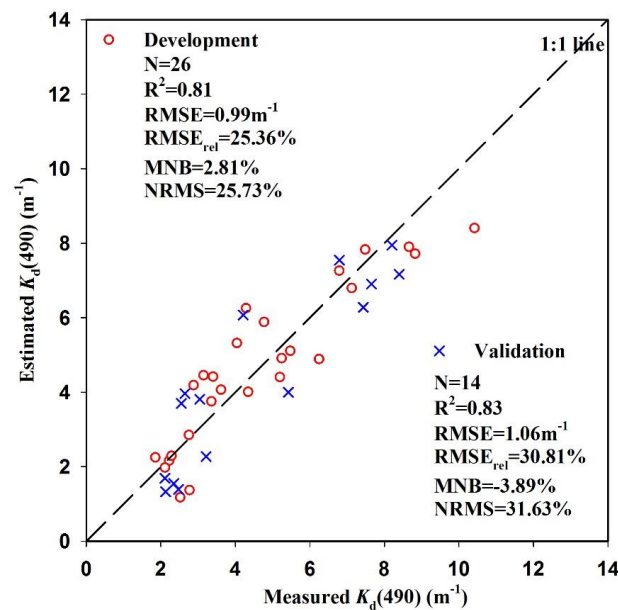


**Figure 5.** Development and validation of the algorithm for estimating  $K_d(490)$  in Lake Taihu from the OLCI-derived  $R_{rs}$ .

#### 3.4. Temporal and Spatial Patterns from the OLCI-Derived $K_d(490)$ in Lake Taihu

The OLCI-derived  $K_d(490)$  data (24 scenes during November 2016–April 2017, Figure 6) were averaged to calculate the  $K_d(490)$  distribution for Lake Taihu (Figure 7a). The  $K_d(490)$  values for all of Lake Taihu ranged from 1.26 to 14.87 m<sup>-1</sup> with a mean value of  $7.11 \pm 2.08$  m<sup>-1</sup>. The  $K_d(490)$  value for southwestern Lake Taihu was highest, followed by  $K_d(490)$  for central Lake Taihu, whereas the  $K_d(490)$  values for the bays were low. The spatial distribution of the coefficients of variation (CV) was calculated from the OLCI-derived  $K_d(490)$  (Figure 7b). The largest  $K_d(490)$  CVs were in Meiliang Bay, followed by Gonghu Bay and Zhushan Bay, and the smallest  $K_d(490)$  CVs were in open areas. Evidently, the distribution of the CVs of  $K_d(490)$  is opposite to that of the values of  $K_d(490)$ ; i.e., high- $K_d(490)$  areas generally have low CV values. In general, the  $K_d(490)$  values for southwestern and central Lake Taihu were high and varied less significantly than those in other areas.

Virtual stations were set up in central Lake Taihu and three typical bay areas, including Zhushan Bay, Meiliang Bay, and Gonghu Bay (S1–S4, Figure 1), to observe and analyze the temporal and spatial differences in  $K_d(490)$  between different areas of the lake. As illustrated in Figure 8, which shows the OLCI-derived  $K_d(490)$  at the four virtual stations,  $K_d(490)$  at station S1 (located in an open area) ( $8.37 \pm 2.31$  m<sup>-1</sup>) is significantly higher than those at the other virtual stations (*t*-test,  $p < 0.05$ ); the  $K_d(490)$  values at stations S2 (located in Zhushan Bay) ( $4.39 \pm 1.81$  m<sup>-1</sup>) and S4 (located in Gonghu Bay) ( $3.86 \pm 1.17$  m<sup>-1</sup>) are the next highest, whereas  $K_d(490)$  at station S3 (located in Meiliang Bay) ( $3.19 \pm 3.86$  m<sup>-1</sup>) is the lowest. The  $K_d(490)$  values at stations S1 and S2 are significantly higher in March than in any other month ( $p < 0.05$ ), which is mainly because the wind speeds are relatively high in March ( $2.47 \pm 0.68$  m/s). There is no significant difference in the  $K_d(490)$  values at the other stations between different months.

In general, the distribution of  $K_d(490)$  for Lake Taihu exhibited significant spatial and temporal variations between November 2016 and April 2017 (Figure 6). By further observing and analyzing OLCI red-green-blue (RGB) images of 24 scenes of Lake Taihu and the corresponding  $K_d(490)$  values, two distribution patterns for  $K_d(490)$  are identified. Type I is the distribution of  $K_d(490)$  under significant bloom coverage (>25% coverage) (e.g., 3 and 6 November and 4 December 2016). Overall,  $K_d(490)$  was low ( $5.01 \pm 1.95$  m<sup>-1</sup>) under these conditions, which is mainly because the wind speeds were low, and almost no wind-induced sediment resuspension occurred during large-scale

outbreaks of algal blooms. In areas with outbreaks of algal blooms, sunlight was blocked by the algae that accumulated on the surface and was unable to penetrate to deeper water. In comparison, in areas without algal blooms, high- $K_d(490)$  areas were mainly distributed near areas with outbreaks of algal blooms, and low- $K_d(490)$  areas were distributed in regions outside the areas with algal bloom outbreaks. Type II is the distribution of  $K_d(490)$  under low bloom coverage (<25% coverage) (e.g., on 15, 16, and 30 December 2016). In general, the  $K_d(490)$  values were high ( $7.60 \pm 2.14 \text{ m}^{-1}$ ) under these conditions. In areas without outbreaks of algal blooms, the high- $K_d(490)$  areas were mainly distributed in southwestern Lake Taihu, followed by central Lake Taihu, whereas the  $K_d(490)$  values for the bay areas were low. It is worth noting that uncertainties of the results for eastern Lake Taihu were due to the effects of aquatic vegetation. Therefore, these results were excluded from the analysis.

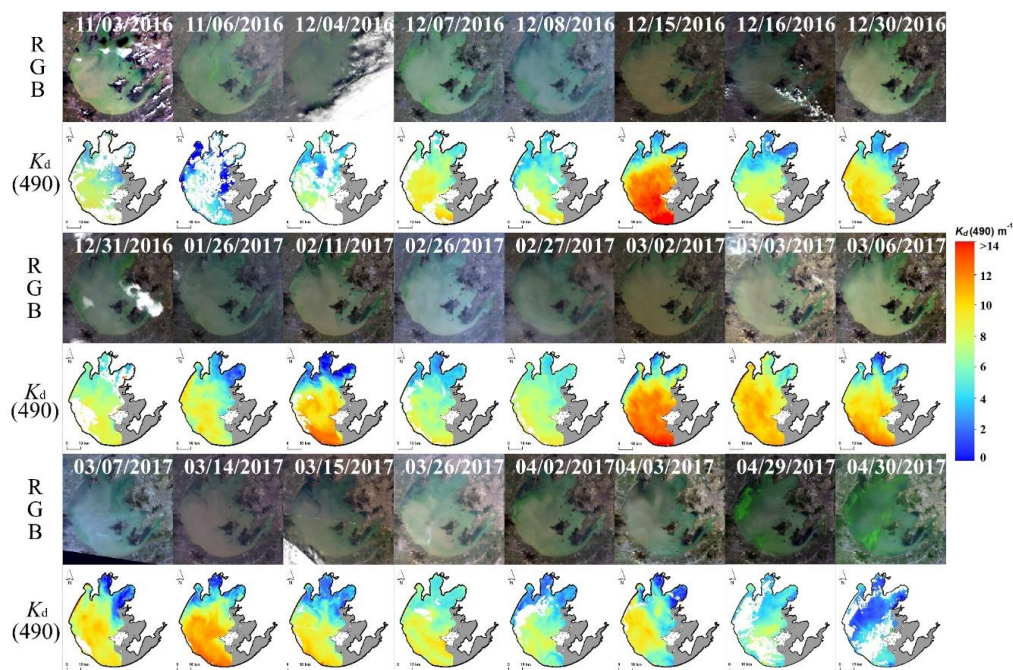


**Figure 6.** Daily OLCI RGB and  $K_d(490)$  distributions in Lake Taihu, China, derived from Sentinel OLCI data (November 2016–April 2017). Note that the data influenced by algal blooms and clouds are excluded.

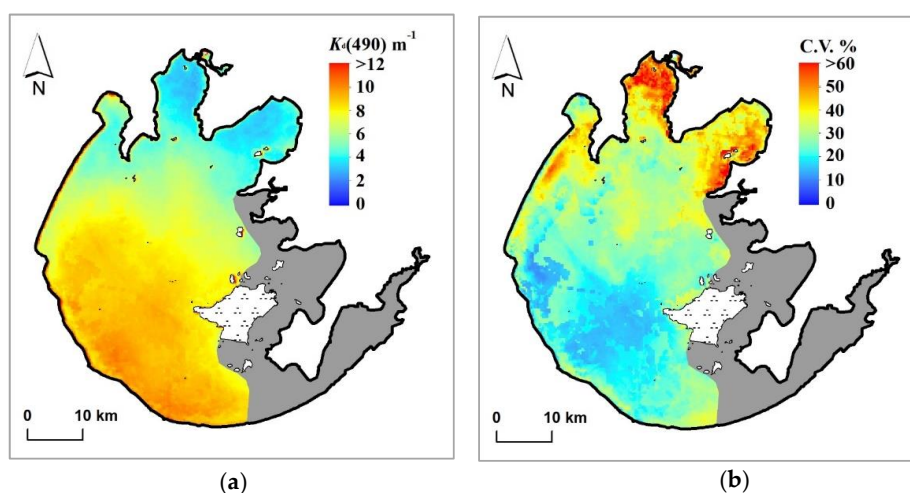


**Figure 7.** Distributions of (a) the mean and (b) the coefficient of variation (CV) of the OLCI-derived  $K_d(490)$  in Lake Taihu from November 2016 to April 2017.

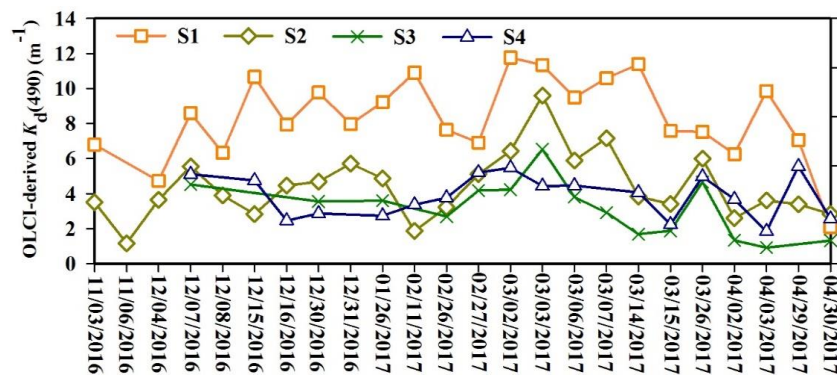


**Figure 8.** Temporal variations of the OLCI-derived  $K_d(490)$  at four virtual stations in different lake segments from November 2016 to April 2017. Note that the data influenced by algal blooms and cloud are excluded.

## 4. Discussion

### 4.1. Performance of the OLCI $K_d(490)$ Algorithm

#### 4.1.1. Challenges in Estimating $K_d(490)$ Using Satellite Data

It is difficult to obtain highly accurate  $R_{rs}$  from satellite images in extremely turbid inland waters due to the complex optical conditions from elevated concentrations of optically active substances and algal blooms [34,53]. This is further complicated when turbid atmospheric conditions from elevated aerosol concentrations are present. The accuracy of estimating the  $R_{rs}$  band ratios is critical to the newly developed  $K_d(490)$  algorithm because the input parameters of this algorithm are two  $R_{rs}$  band ratios ( $R_{rs}(681)/R_{rs}(560)$  and  $R_{rs}(754)/R_{rs}(560)$ ). The sensitivity of this algorithm to the input parameters was analyzed (Figure 9a), and the results indicate that this algorithm is highly sensitive to  $R_{rs}(681)/R_{rs}(560)$  and less sensitive to  $R_{rs}(754)/R_{rs}(560)$ . The  $RMSE_{rel}$  of  $K_d(490)$  increases to 64.32% when  $R_{rs}(681)/R_{rs}(560)$  is underestimated or overestimated by 30%, whereas it increases to 24.49% when  $R_{rs}(754)/R_{rs}(560)$  is underestimated or overestimated by 30%. Fortunately, the accuracies of the two  $R_{rs}$  band ratios are quite high (Figure 9b;  $R^2 > 0.65$ ,  $RMSE_{rel} < 39.00\%$ ,  $MNB < 27.00\%$  and  $NRMS < 29.00\%$ ), especially that of the  $R_{rs}(681)/R_{rs}(560)$  band ratio ( $R^2 = 0.86$ ,  $RMSE_{rel} = 13.58\%$ ,  $MNB = 3.79\%$  and  $NRMS = 13.18\%$ ), as the  $R_{rs}$  band ratios can decrease the effect of the atmospheric correction [54]. In general, the effects of the atmospheric correction's uncertainty are small, and the 6S atmospheric correction for the OLCI over Lake Taihu is considered to be appropriate for us to focus our study on the retrieval and validation of  $K_d(490)$ .

Atmospheric correction was also performed based on the aerosol parameters measured at an AERONET station in conjunction with the 6S radiative transfer model. However, aerosols were measured at only one station near Meiliang Bay (Figure 1). As a result, the measurements cannot effectively characterize the distribution of aerosols across all of Lake Taihu, which will also affect the accuracy of the results obtained from the atmospheric correction and estimation of  $K_d(490)$ . Here, we use the measurements taken on 14 March 2017, as an example. On this date, the AOD(550) acquired at the AERONET station is 0.3493. Let us assume that the actual AOD(550) ranges from 0.1 to 1.5 (Figure 9c,d). The OLCI-derived  $R_{rs}$  band ratios ( $R_{rs}(681)/R_{rs}(560)$  and  $R_{rs}(754)/R_{rs}(560)$ ) and the OLCI-derived  $K_d(490)$  both increase as the input AOD(550) increases. When  $AOD(550) > 1.0$ ,  $K_d(490)$  increases rapidly as AOD(550) increases, the absolute relative error ( $abs(K_d(490)_{AERONET} - K_d(490)_{simulation}) / K_d(490)_{AERONET}$ ) also increases rapidly. When  $0.1 < AOD(550) < 0.8$  (within the spatial variation for Lake Taihu), the absolute relative error is within 10% and is thus acceptable.



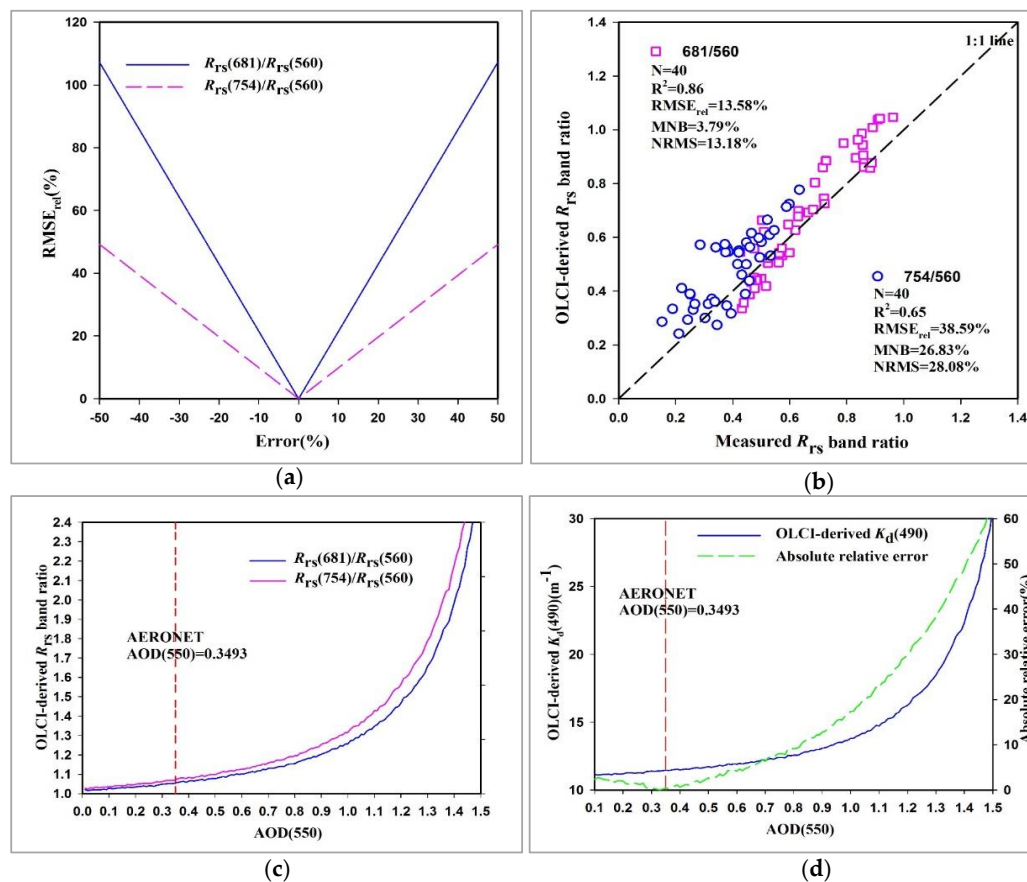


**Figure 9.** (a) Variation of  $RMSE_{rel}$  for  $K_d(490)$  derived from the errors introduced by  $R_{rs}(681)/R_{rs}(560)$  and  $R_{rs}(754)/R_{rs}(560)$  from the atmospheric correction; (b) comparison of the in situ measured  $R_{rs}$  band ratios and the OLCI-derived  $R_{rs}$  band ratios after the 6S atmospheric correction for  $R_{rs}(681)/R_{rs}(560)$  and  $R_{rs}(754)/R_{rs}(560)$ ; (c,d) examples showing the influence of the aerosol optical depth on the OLCI-derived  $R_{rs}$  band ratios/ $K_d(490)$  at virtual station S1 on 14 March 2017.

#### 4.1.2. Comparison with Existing Algorithms Using the OLCI-Derived $R_{rs}$

We evaluated the published empirical algorithms proposed by Muller [21], Kratzer et al. [22], and Wang et al. [20], in addition to a semi-analytical algorithm proposed by Lee et al. [4] based on satellite-in situ matchups. Due to the significant differences in the bio-optical properties of different waters, we first calibrated the coefficients for these empirical algorithms using the calibration data set from Lake Taihu.

The blue-green band ratio (490/560) algorithm commonly used for oceanic waters [21] had a relatively low estimation accuracy ( $R^2 = 0.34$ ,  $RMSE = 1.88 m^{-1}$ ,  $RMSE_{rel} = 47.39\%$ ,  $MNB = 15.89\%$  and  $NRMS = 45.21\%$ ) (Table 2). This is mainly because  $K_d(490)$  for the waters of Lake Taihu is mainly controlled by the SPM in the waters and is insignificantly related to the Chla concentration. The blue-red band ratio (490 nm/620 nm) algorithm suitable for coastal waters [22] also had a low estimation accuracy ( $R^2 = 0.02$ ,  $RMSE = 2.30 m^{-1}$ ,  $RMSE_{rel} = 64.00\%$ ,  $MNB = 25.95\%$  and  $NRMS = 59.25\%$ ). This is mainly because the absorption peak of microcystis aeruginosa, which is the main algal species in Lake Taihu, occurs at 620 nm, so the blue-red band ratio cannot accurately reflect information about the SPM in the waters of Lake Taihu. The red-blue band ratio (674 nm/490 nm) algorithm [20] had a relatively high estimation accuracy ( $R^2 = 0.71$ ,  $RMSE = 1.26 m^{-1}$ ,  $RMSE_{rel} = 34.68\%$ ,  $MNB = 7.28\%$  and  $NRMS = 34.34\%$ ). However, this algorithm uses the blue band (490 nm), which is associated with significant uncertainties regarding the atmospheric correction accuracy for turbid inland waters. Therefore, this algorithm is not recommended for use to derive



$K_d(490)$  for the waters of turbid inland lakes from remote sensing data. The dual band ratio (681 nm/560 nm and 754 nm/560 nm) algorithm developed in this study had a high estimation accuracy ( $R^2 = 0.81$ ,  $RMSE = 0.99 \text{ m}^{-1}$ ,  $RMSE_{rel} = 25.36\%$ ,  $MNB = 2.81\%$  and  $NRMS = 25.73\%$ ). This is because the NIR, red, and green bands are the key bands for deriving the water quality parameters of inland waters from remote sensing data [25], particularly for deriving Chla and SPM concentrations [55–57].

The single band ratio (681 nm/560 nm) algorithm also had a relatively high estimation accuracy ( $R^2 = 0.66$ ,  $RMSE = 1.32 \text{ m}^{-1}$ ,  $RMSE_{rel} = 31.58\%$ ,  $MNB = 6.41\%$  and  $NRMS = 31.56\%$ ). However, large uncertainties were associated with the estimation results obtained using this algorithm for Lake Taihu, which had a wide distribution of algae. Figure 10 shows the estimates of  $K_d(490)$  on April 29, 2017 that were obtained using the single band ratio algorithm and the dual band ratio algorithm. The estimates obtained using these two algorithms were generally consistent with one another in areas without algal blooms (mean values of  $5.26 \pm 1.20$  and  $5.67 \pm 2.16 \text{ m}^{-1}$ , respectively). However, there was a large difference between the estimates of  $K_d(490)$  in algal bloom-covered areas and areas with high algal particle concentrations in the periphery (red circles in Figure 10a). Evidently, the single band ratio algorithm significantly underestimated  $K_d(490)$  for algal bloom-covered waters (Figure 10b), whereas the estimates obtained using the dual band ratio algorithm were too high (Figure 10c). The estimates obtained using the dual band ratio algorithm were more consistent with the actual conditions. This is because as the amount of planktonic algae in the water increases, the  $R_{rs}$  value of the water at 560 nm also increases due to the impacts of the low absorption of phytoplankton pigments and scattering by algal cells, whereas the  $R_{rs}$  value of the water at 681 nm decreased as a result of the absorption by Chla [58,59]; consequently, the 681-nm/560-nm band ratio decreased, which in turn led to an underestimation. Because the reflection of water at 754 nm mainly relies on the SPM concentration and is the least sensitive to algal pigments [60], the effects of changes in the algal concentration can be reduced by using another band ratio (754 nm/560 nm) to compensate for the deficiency in the 681-nm/560-nm band ratio. Although algal bloom-covered areas were mostly masked off in research on the estimation of  $K_d$  [61], it was difficult to completely remove these areas in practice; in addition, the algal particle concentrations in the waters surrounding the algal bloom-covered areas were still high. Therefore, the dual band ratio algorithm was more suitable for eutrophic lakes with a wide distribution of algae.

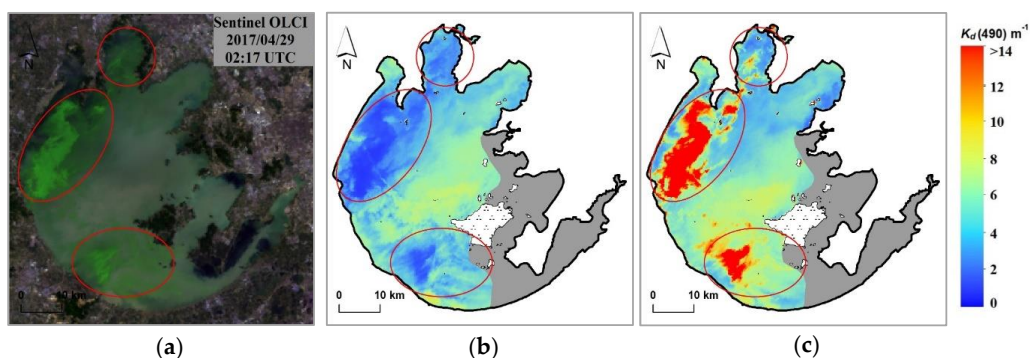


**Figure 10.** (a) The OLCI RGB image, (b) the single band ratio algorithm-derived  $K_d(490)$ , and (c) the dual band ratio algorithm-derived  $K_d(490)$  from the OLCI for 29 April 2017.

**Table 2.** Comparison of the performance of the existing and proposed  $K_d(490)$  estimation algorithms using the OLCI-derived  $R_{rs}$ .

Type	Equation	$R^2$	RMSE/m <sup>-1</sup>	RMSE <sub>rel</sub> /m <sup>-1</sup>	MNB/%	NRMS/%	Reference
Empirical algorithm	$K_d(490) = 0.022 + 8.79 * \left[ \frac{R_{rs}(490)}{R_{rs}(560)} \right]^{1.72}$	0.34	1.88	47.39	15.89	45.21	[21]
	$K_d(490) = 0.022 + \exp[-1.05 * \ln(R_{rs}(490)/R_{rs}(620)) + 1.42]$	0.02	2.30	64.00	25.95	59.25	[22]
	$K_d(490) = 18.53 * \frac{R_{rs}(674)}{R_{rs}(490)} - 12.37$	0.71	1.26	34.68	7.28	34.34	[20]
Semi-analytical algorithm	$K_d(490) = (1 + 0.005 * \theta_0) * a(490) + 4.18 * [1 - 0.52 * e^{-10.08 * a(490)}] * b_b(490)$	0.43	2.86	47.55	-45.25	14.79	[4]
This study	$K_d(490) = 11.89 * \frac{R_{rs}(681)}{R_{rs}(560)} + 6.81 * \frac{R_{rs}(754)}{R_{rs}(560)} - 6.17$	0.81	0.99	25.36	2.81	25.73	-

Note: The parameters in the empirical algorithm are re-parameterized with the in situ measurement data from Lake Taihu;  $\theta_0$  is the above surface solar zenith angle, and  $a(490)$  and  $b_b(490)$  are the total absorption coefficient and backscattering coefficient at 490 nm, respectively, retrieved by the Quasi-Analytical Algorithm (QAA) [62].

The semi-analytical algorithm is a semi-analytical model for  $K_d$  that was established by solving  $a$  and  $b_b$  based on a numerical solution of the radiative transfer model [4,18]. Lee et al. used a multiband quasi-analytical algorithm (QAA) to derive the absorption and backscattering coefficients of water from remote sensing data [62] and then determine  $K_d(490)$  based on its relationships with the absorption and backscattering coefficients. However, the QAA had a low accuracy ( $R^2 = 0.43$ ,  $RMSE = 2.86 \text{ m}^{-1}$ ,  $RMSE_{rel} = 47.55\%$ ,  $MNB = -45.25\%$  and  $NRMS = 14.79\%$ ). This was mainly because the empirical steps involved in this algorithm were unsuitable for type II inland waters with complex optical properties [23], resulting in large errors in the estimation of the inherent optical properties that were eventually passed to the  $K_d(490)$  estimate. As a result, the estimation accuracy of the QAA was lower than that of the empirical algorithm. In contrast, the dual band ratio (681 nm/560 nm and 754 nm/560 nm) algorithm had a high estimation accuracy and is therefore suitable for estimating  $K_d(490)$  for waters of turbid inland lakes based on remote sensing data.

#### 4.1.3. Applicability of the Algorithm to Other Lakes

To examine its wider applicability, the dual band ratio (681 nm/560 nm and 754 nm/560 nm) algorithm was applied to Lake Chaohu, which is the fifth largest freshwater lake in China and is a typical eutrophic lake [63,64]. A total of 23 synchronous satellite and ground data points for Lake Chaohu were obtained by following the synchronous satellite and ground data matching criteria. The estimation accuracy of the dual band ratio algorithm was found to be low when it was used directly with the Lake Chaohu data (Figure 11a;  $R^2 = 0.60$ ,  $RMSE = 1.38 \text{ m}^{-1}$  and  $MAPE = 21.85\%$ ), and the intersection points between the estimated and measured values of  $K_d(490)$  are generally below the 1:1 line. This is because the coefficient of the algorithm was obtained by empirical regression based on the Lake Taihu data. Thus, the parameters of the algorithm for Lake Taihu were calibrated against the Lake Chaohu data. As a result, the estimation accuracy of the algorithm was improved significantly (Figure 11b;  $R^2 = 0.80$ ,  $RMSE = 0.54 \text{ m}^{-1}$  and  $MAPE = 7.55\%$ ), and the intersection points between the estimated and measured values of  $K_d(490)$  were generally distributed near the 1:1 line; in addition, a reasonable spatial distribution of  $K_d(490)$  can be observed by comparing the RGB images (Figure 11c,d). Therefore, the dual band ratio algorithm developed in this study exhibits high applicability for turbid inland waters; however, its coefficient must be re-parameterized based on the optical properties of the study waters.

#### 4.2. Comparison between the OLCI-Derived and MODIS-Derived $K_d(490)$

To further confirm the accuracy of the spatial distribution of the OLCI-derived  $K_d(490)$  values, the  $K_d(490)$  values for Lake Taihu derived from Terra-MODIS using a newly proposed  $K_d(490)$  semi-analytical algorithm [61] were used as quasi-reference values and compared with those derived from Sentinel-3A-OLCI. A total of 18 OLCI-MODIS image matchups were used, and six matchups with large uncertainties in the MODIS atmospheric correction were excluded. The distribution of the RMSEs is shown in Figure 12a. The mean RMSE is  $2.40 \pm 1.02 \text{ m}^{-1}$ , which indicates high consistency. However, it is also worth noting that large errors occur in the land-water regions due to border effects. The MODIS-derived  $K_d(490)$  values were resampled to a spatial resolution of 300 m, which is the same as that of the OLCI. Figure 12b shows a pixel-by-pixel scatter plot between all of the  $K_d(490)$  products from the OLCI and MODIS. Significant correlations between the OLCI-derived and MODIS-derived  $K_d(490)$  values were observed ( $r = 0.75$ ,  $p < 0.001$ ,  $N = 292,970$ ):

$$K_d(490)_{OLCI} = 0.62 \times K_d(490)_{MODIS} - 2.52 \quad (4)$$

where  $K_d(490)_{OLCI}$  and  $K_d(490)_{MODIS}$  are the OLCI-derived and MODIS-derived  $K_d(490)$  values, respectively. These results indicate good agreement between the OLCI-derived and MODIS-derived  $K_d(490)$  values.

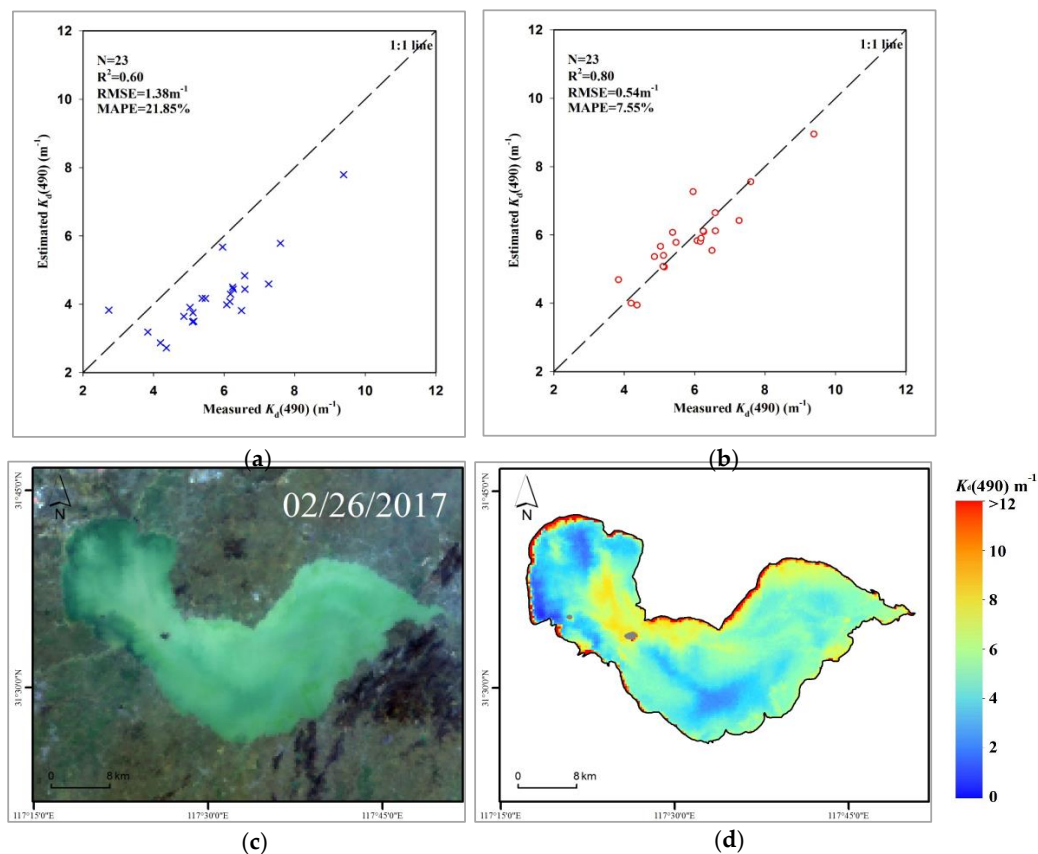


**Figure 11.** (a,b) Validation of the algorithm for estimating  $K_d(490)$  in Lake Chaohu using the OLCI-derived  $R_{rs}$  with the default parameterization and local parameterization; (c,d) OLCI RGB and OLCI-derived  $K_d(490)$  distributions in Lake Chaohu on 26 February 2017.

For additional detail, the OLCI- and MODIS-derived  $K_d(490)$  values on 14 March 2017 and 29 April 2017, which represent the typical  $K_d(490)$  patterns in Lake Taihu under low bloom coverage conditions and significant bloom coverage conditions, respectively, were compared (Figure 13a,b). The general patterns of  $K_d(490)$  were consistent with each other, especially under low bloom coverage conditions (Figure 13c,d). However, the OLCI-derived  $K_d(490)$  exhibited a smoother spatial distribution and finer textual characteristics, whereas the MODIS-derived  $K_d(490)$  had a noisy pattern. This is because the OLCI has a higher spatial and radiation resolution and a higher signal-to-noise ratio (ANR) than MODIS. Figure 13(e1,f1) show the distributions of the absolute relative differences (ARE;  $\text{abs}(K_d(490)_{\text{OLCI}} - K_d(490)_{\text{MODIS}}) / K_d(490)_{\text{MODIS}}$ ) between the OLCI-derived and MODIS-derived  $K_d(490)$  values. The mean absolute relative differences on 14 March 2017 and 29 April 2017 were  $19.79 \pm 16.83\%$  and  $20.84 \pm 21.79\%$ , respectively. There was good consistency between the spatial distributions of the OLCI-derived and MODIS-derived  $K_d(490)$  values on 14 March 2017 (Figure 13(e1)) in all areas except for Meiliang Bay and Zhushan Bay, where there are large differences. In addition, there is generally good consistency between the spatial distributions of the OLCI-derived and MODIS-derived  $K_d(490)$  values on 29 April 2017 (Figure 13(f1)) in all areas except for the bank areas, where there are large differences. To evaluate the consistency between the two satellite-derived  $K_d(490)$  products, pixel-by-pixel scatter plots of the  $K_d(490)$  values derived from the OLCI against those from MODIS are shown in Figure 13(e2,f2). The OLCI-derived and MODIS-derived  $K_d(490)$  values are significantly correlated with each other, and the Pearson correlation coefficients ( $r$ ) on 14 March 2017 and 29 April 2017 are 0.93 and 0.43, respectively, ( $p < 0.001$ ). The Pearson correlation coefficient under significant bloom coverage conditions (29 April 2017) is low. Large errors occurred in both non-algal bloom-based algorithms due to adjacency effects of algal bloom areas and non-algal bloom areas.



However, most of the pixels were distributed along the 1:1 line. These results further demonstrate that the dual band ratio algorithm and OLCI images are suitable for  $K_d(490)$  estimation.

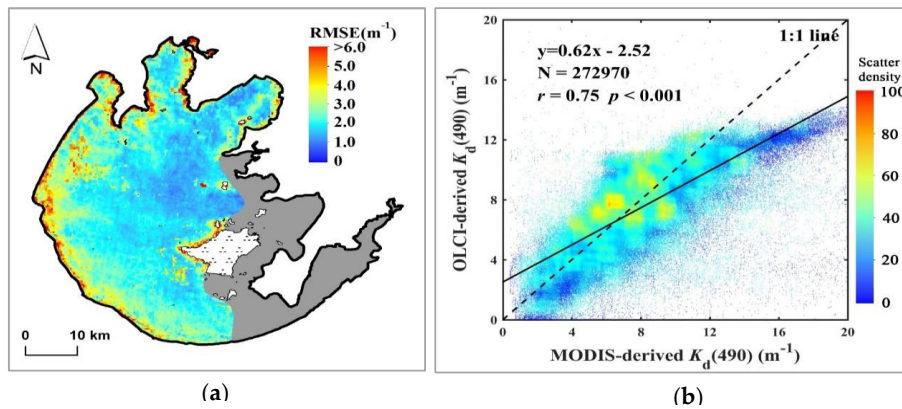


**Figure 12.** Distribution of the RMSE (a) and pixel-by-pixel scatter plot (b) between all of the  $K_d(490)$  products from the OLCI and MODIS. A total of 18 OLCI-MODIS image matchups were used, and six matchups with large uncertainties in the MODIS atmospheric correction were excluded. Note that bad pixels were removed.

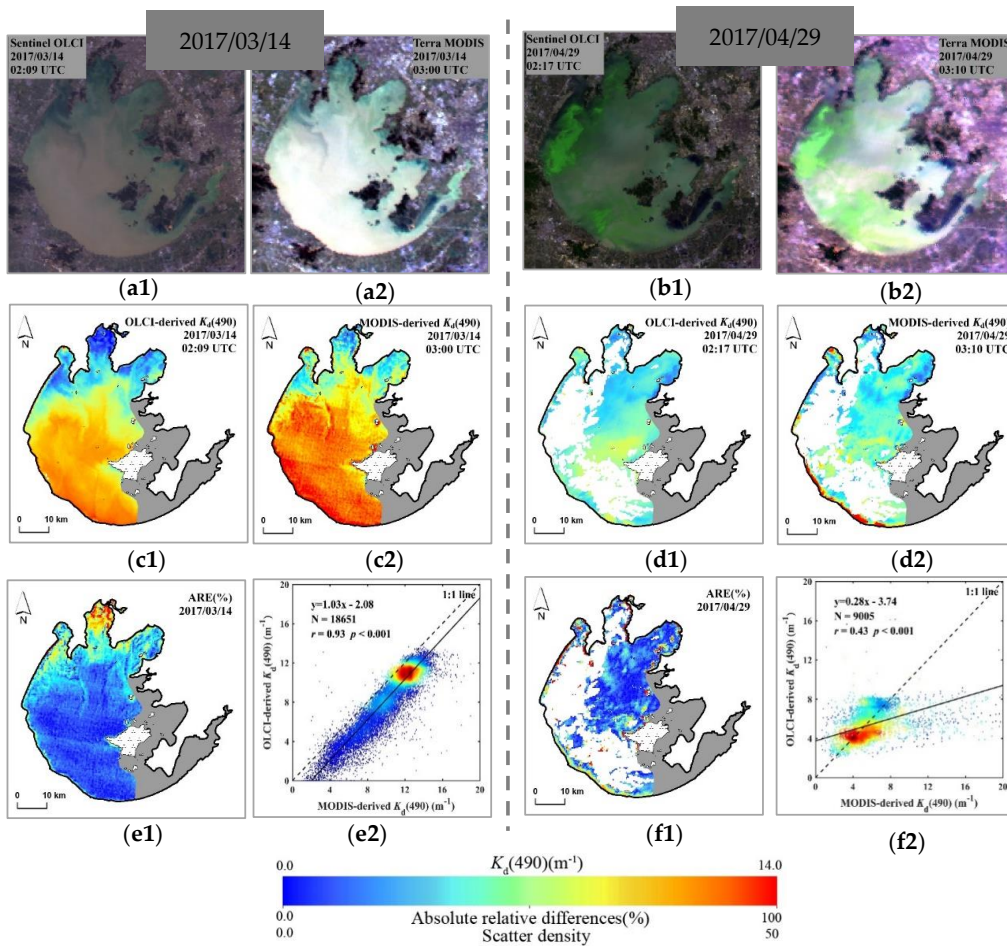


**Figure 13.** (a,b) OLCI and MODIS RGB images, (c,d) OLCI- and MODIS-derived  $K_d(490)$  values, (e,f) absolute relative differences (ARE) and pixel-by-pixel scatter plots between the  $K_d(490)$  products from the OLCI and MODIS on 14 March 2017, and 29 April 2017. Note that bad pixels were removed.



Overall, there is good consistency between the OLCI-derived and MODIS-derived  $K_d(490)$  values. However, because the OLCI has higher spatial and radiometric resolutions and a higher ANR, the OLCI provides more detailed information for future monitoring of the water quality of inland waters.

#### 4.3. Mechanisms of the Spatio-Temporal Variations in the $K_d(490)$ Distribution

Our study shows that in the absence of algal blooms, the changes in  $K_d(490)$  for the waters of Lake Taihu are mainly caused by changes in SPM, especially the changes in SPIM. An increase in the SPM concentration results in an increase in the light attenuation in the water, which results in a decrease in the transparency and eutrophic depth of the water and thereby affects the spatial and seasonal distributions of aquatic vegetation [65,66]. As a shallow lake, the high dynamic ratio index (the square root of the surface area divided by the average depth, 25.6 km/m) of Lake Taihu indicates that winds are the main driving force for sediment resuspension. Wind- and wave-induced sediment resuspension will increase the SPM concentration in the water and thereby increase light attenuation in the water [52,67,68]. Several studies have demonstrated that the wind-induced resuspension is important in sediment related turbulence, the main driving factor for the spatial and temporal variations in  $K_d$  for Lake Taihu [27,61,69].

To further examine the effects of wind on the spatial distribution of  $K_d(490)$ , we analyzed the relationships between the OLCI-derived  $K_d(490)$  values and the mean wind speeds pixel by pixel at different times before the acquisition of the remote sensing image (Figure 14). Taking the four virtual stations as an example (Figure 14a), the Pearson correlation coefficient ( $r$ ) between the OLCI-derived  $K_d(490)$  and the mean wind speed for different hours ( $h = 1, 2, 3, \dots, 96$  h) before the satellite image acquisition time was calculated, and the maximum Pearson correlation coefficient ( $r$ ) and corresponding hours were then determined and recorded. The maximum Pearson correlation coefficient ( $r$ ) can indicate the influence of the wind speed on  $K_d(490)$ , and the corresponding hours can indicate the duration of the wind speed effect on  $K_d(490)$ . The maximum correlation coefficients at stations S1–S4 are 0.56, 0.39, 0.43, and 0.46 ( $p < 0.05$ ), which correspond to 50, 14, 11, and 15 h, respectively. This indicates that the wind speed has the longest lasting effect and a significant impact on  $K_d(490)$  at station S1 and insignificant and short impacts on  $K_d(490)$  at stations S2–S4. This is because station S1 (located in central Lake Taihu) is more prone to wind effects, which can lead to sediment resuspension, whereas stations S2–S4 (located in the bay areas) are relatively closed, and the wind speed has an insignificant impact on sediment resuspension at these stations. In addition, the time delay for waves resulting from a change in the wind field varies between different waters, and the bay areas tend to stabilize before central Lake Taihu [68].

Figure 14b shows the spatial distribution of the maximum correlation coefficients. The correlation coefficient is the highest ( $r \approx 0.6$ ,  $p < 0.05$ ) in central Lake Taihu, followed by Gonghu Bay and Meiliang Bay ( $r \approx 0.4$ ,  $p < 0.05$ ), which indicates that the wind speed has a greater impact on  $K_d(490)$  in central Lake Taihu than in the bay areas. No significant statistical correlations are found in southwestern and northwestern Lake Taihu and in Zhushan Bay ( $r \approx 0.2$ ,  $p < 0.05$ ), which indicates that wind speed-induced sediment resuspension is not the only factor that affects the SPM concentration in these areas; the sediment distribution, lake currents, precipitation, and runoff can all affect the SPM concentration [70] and thereby affect  $K_d(490)$ . Figure 14c shows the spatial distribution of the numbers of hours corresponding to the highest correlation. Southwestern Lake Taihu corresponds to the largest number of hours ( $>80$  h), central Lake Taihu corresponds to a relatively large number of hours ( $>48$  h), and the bay areas correspond to a few hours ( $<15$  h). This indicates that winds have the longest impact on  $K_d(490)$  in southwestern Lake Taihu, followed by central Lake Taihu, and a short impact on the  $K_d(490)$  in the bay areas.

Overall, wind- and wave-induced sediment resuspension is the main driving force for changes in  $K_d(490)$  in the waters of Lake Taihu in the absence of algal blooms and has a longer impact on  $K_d(490)$  in central Lake Taihu than in the bay areas. Note that heavy rainfall events may have a great impact on the  $K_d(490)$  of Lake Taihu through rivers plums [61,70,71]. But unfortunately, we did not observe this

phenomenon due to the unavailability of OLCI data during precipitation events. Another factor is the increased occurrence of massive algal blooms in the lake, a result of the rapid urbanization and industrialization of the Lake Taihu basin in recent years [34,72], increasing  $K_d(490)$  dramatically.

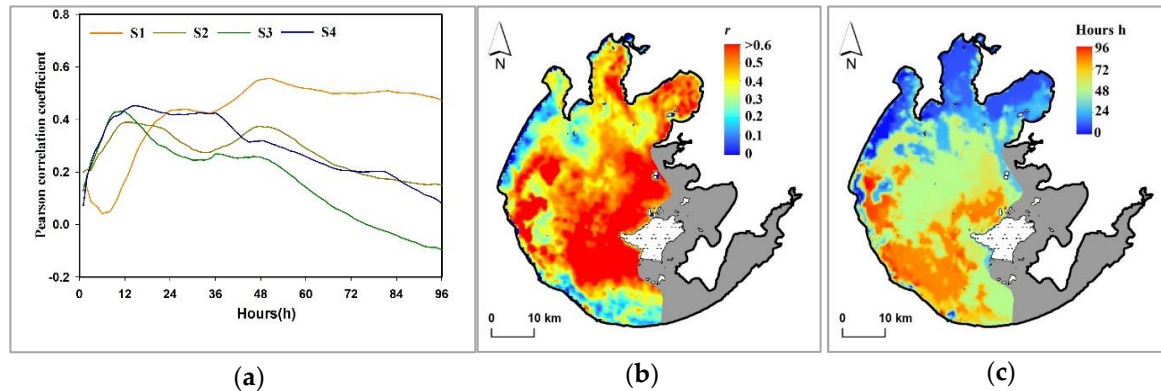


**Figure 14.** (a) Pearson correlation coefficients ( $r$ ) between the OLCI-derived  $K_d(490)$  and the mean wind speed for different hours ( $h = 1, 2, 3, \dots, 96$  h) before the satellite image acquisition time at 4 virtual stations; (b) distribution of the maximum Pearson correlation coefficients ( $r$ ); (c) distribution of hours corresponding to the maximum Pearson correlation coefficients.

## 5. Conclusions

Using Sentinel-3A-OLCI data, satellite monitoring of  $K_d(490)$  for the waters of Lake Taihu was achieved for the first time since this satellite was put into operation in October 2016. The patterns of and driving factors for the spatial and temporal variations results show that  $K_d(490)$  is the highest in southwestern Lake Taihu, followed by central Lake Taihu, and that  $K_d(490)$  is relatively low in the bay areas. Wind- and wave-induced sediment resuspension is the main factor that affects the variations in  $K_d(490)$ . Moreover, winds have a longer impact on  $K_d(490)$  in central Lake Taihu than in the bay areas because winds and waves tend to stabilize in the bay areas before central Lake Taihu.

This study also showed that SPIM controls the underwater light attenuation and distribution in the waters of Lake Taihu through absorption and scattering, which affect the transparency and eutrophic depth of the water and consequently the variations in the seasonal and spatial distributions of aquatic vegetation. Based on synchronous satellite and ground datasets, a novel dual band ratio (681 nm/560 nm and 754 nm/560 nm) algorithm was found to accurately estimate  $K_d(490)$  for turbid inland waters. The development of new algorithms that take advantage of the improved radiometric and spatial resolution of OLCI data will increase in the coming years. Compared to available algorithms, the algorithm developed in this study has a higher accuracy and can reduce the effects of atmospheric and environmental factors.

Satellite imagery improves our understanding of the characteristics of the photoecological environments in water and thereby supports the evaluation and management of lake water quality. In future work, data acquired by multiple satellite sensors, such as MERIS, MODIS, and OLCI, can be used to determine the historical evolution of  $K_d(490)$  for inland turbid waters. Considering the highly dynamic variations in the waters of Lake Taihu, high temporal-resolution Geostationary Ocean Color Imager (South Korea) and GaoFen-4 (China) satellite data and meteorological and hydrological data can be used to further understand the evolution of spatial patterns in the photoecological environment over short time scales. In summary, we believe that the addition of OLCI data will provide more possibilities for monitoring, evaluating, and managing lake water quality.

**Acknowledgments:** The authors would like to thank all of the study participants and volunteer contributors (Jing Li, Dian Wang, Qichun Liang, Yixuan Zhang, and Tianci Qi [Nanjing Institute of Geography and Limnology, Chinese Academy of Sciences: NIGLAS]). We also thank ESA and NASA for providing the satellite data and processing software. Financial support was provided by the Provincial Natural Science Foundation of Jiangsu,

China (BK20160049), the National Natural Science Foundation of China (41671358, 41431176), the Youth Innovation Promotion Association of CAS (2012238) and Dragon 4.

**Author Contributions:** H.D. principally conceived of the idea for the study. M.S. was responsible for setting up the experiments, completing the experiments, and retrieving the data. Z.C., K.X., S.L., and H.Y. contributed to the analysis and discussion. M.S. and H.D. finalized the manuscript. All of the authors participated in some form in the concept, experimentation, writing, and/or editing of this manuscript.

**Conflicts of Interest:** The authors declare no conflict of interest.

## References

- Gordon, H.R. Dependence of the diffuse reflectance of natural waters on the sun angle. *Limnol. Oceanogr.* **1989**, *34*, 1484–1489. [[CrossRef](#)]
- Gordon, H.R.; Brown, O.B.; Jacobs, M.M. Computed relationships between the inherent and apparent optical properties of a flat homogeneous ocean. *Appl. Opt.* **1975**, *14*, 417–427. [[CrossRef](#)] [[PubMed](#)]
- Baker, K.; Smith, R. Quasi-Inherent Characteristics of the Diffuse Attenuation Coefficient for Irradiance. *Proc. SPIE* **1980**. [[CrossRef](#)]
- Lee, Z.P.; Du, K.P.; Arnone, R. A model for the diffuse attenuation coefficient of downwelling irradiance. *J. Geophys. Res. Oceans* **2005**, *110*. [[CrossRef](#)]
- Mobley, C.D. *Light and Water: Radiative Transfer in Natural Waters*; Academic Press: Cambridge, MA, USA, 1994.
- Kirk, J. Monte carlo study of the nature of the underwater light field in, and the relationships between optical properties of, turbid yellow waters. *Mar. Freshw. Res.* **1981**, *32*, 517–532. [[CrossRef](#)]
- Majozi, N.P.; Salama, M.S.; Bernard, S.; Harper, D.M.; Habte, M.G. Remote sensing of euphotic depth in shallow tropical inland waters of Lake Naivasha using meris data. *Remote Sens. Environ.* **2014**, *148*, 178–189. [[CrossRef](#)]
- Ma, R.; Tang, J.; Dai, J.; Zhang, Y.; Song, Q. Absorption and scattering properties of water body in Taihu lake, China: Absorption. *Int. J. Remote Sens.* **2006**, *27*, 4277–4304. [[CrossRef](#)]
- Stramska, M.; Zuzewicz, A. Influence of the parametrization of water optical properties on the modelled sea surface temperature in the Baltic sea. *Oceanologia* **2013**, *55*, 53–76. [[CrossRef](#)]
- Wu, Y.; Tang, C.C.; Sathyendranath, S.; Platt, T. The impact of bio-optical heating on the properties of the upper ocean: A sensitivity study using a 3-d circulation model for the Labrador sea. *Deep Sea Res. Part II Top. Stud. Oceanogr.* **2007**, *54*, 2630–2642. [[CrossRef](#)]
- Loiselle, S.A.; Bracchini, L.; Cózar, A.; Dattilo, A.M.; Tognazzi, A.; Rossi, C. Variability in photobleaching yields and their related impacts on optical conditions in subtropical lakes. *J. Photochem. Photobiol. B Biol.* **2009**, *95*, 129–137. [[CrossRef](#)] [[PubMed](#)]
- McClain, C.R.; Arrigo, K.; Tai, K.S.; Turk, D. Observations and simulations of physical and biological processes at ocean weather station P, 1951–1980. *J. Geophys. Res.* **1996**, *101*, 3697–3713. [[CrossRef](#)]
- Bergamino, N.; Horion, S.; Stenuite, S.; Cornet, Y.; Loiselle, S.; Plisnier, P.D.; Descy, J.P. Spatio-temporal dynamics of phytoplankton and primary production in Lake Tanganyika using a MODIS based bio-optical time series. *Remote Sens. Environ.* **2010**, *114*, 772–780. [[CrossRef](#)]
- Lee, Z.; Lance, V.P.; Shang, S.; Vaillancourt, R.; Freeman, S.; Lubac, B.; Hargreaves, B.R.; Castillo, C.D.; Miller, R.; Twardowski, M. An assessment of optical properties and primary production derived from remote sensing in the southern ocean (so gasex). *J. Geophys. Res.* **2011**, *116*, 111–121. [[CrossRef](#)]
- Austin, R.W.; Petzold, T.J. *The Determination of the Diffuse Attenuation Coefficient of Sea Water Using the Coastal Zone Color Scanner*; Springer: New York, NY, USA, 1981; pp. 239–256.
- Morel, A.; Huot, Y.; Gentili, B.; Werdell, P.J.; Hooker, S.B.; Franz, B.A. Examining the consistency of products derived from various ocean color sensors in open ocean (case 1) waters in the perspective of a multi-sensor approach. *Remote Sens. Environ.* **2007**, *111*, 69–88. [[CrossRef](#)]
- Lee, Z.; Hu, C.; Shang, S.; Du, K.; Lewis, M.; Arnone, R.; Brewin, R. Penetration of uv-visible solar radiation in the global oceans: Insights from ocean color remote sensing. *J. Geophys. Res. Oceans* **2013**, *118*, 4241–4255. [[CrossRef](#)]

18. Lee, Z.P.; Darecki, M.; Carder, K.L.; Davis, C.O.; Stramski, D.; Rhea, W.J. Diffuse attenuation coefficient of downwelling irradiance: An evaluation of remote sensing methods. *J. Geophys. Res. Oceans* **2005**, *110*, 93–106. [[CrossRef](#)]
19. Doron, M.; Babin, M.; Mangin, A.; Hembise, O. Estimation of light penetration, and horizontal and vertical visibility in oceanic and coastal waters from surface reflectance. *J. Geophys. Res. Oceans* **2007**, *112*, 137–154. [[CrossRef](#)]
20. Wang, M.; Son, S.; Harding, L.W. Retrieval of diffuse attenuation coefficient in the Chesapeake Bay and turbid ocean regions for satellite ocean color applications. *J. Geophys. Res. Oceans* **2009**, *114*. [[CrossRef](#)]
21. Mueller, J.L. SeaWiFS algorithm for the diffuse attenuation coefficient,  $k(490)$ , using water-leaving radiances at 490 and 555 nm. In *SeaWiFS postlaunch Calibration and Validation Analyses*; BiblioGov: Columbus, OH, USA, 2000; Volume 3, pp. 24–27.
22. Kratzer, S.; Brockmann, C.; Moore, G. Using MERIS full resolution data to monitor coastal waters—A case study from Himmerfjärden, a fjord-like bay in the northwestern Baltic Sea. *Remote Sens. Environ.* **2008**, *112*, 2284–2300. [[CrossRef](#)]
23. Zhang, Y.; Liu, X.; Yin, Y.; Wang, M.; Qin, B. A simple optical model to estimate diffuse attenuation coefficient of photosynthetically active radiation in an extremely turbid lake from surface reflectance. *Opt. Express* **2012**, *20*, 20482–20493. [[CrossRef](#)] [[PubMed](#)]
24. Qiu, Z.; Wu, T.; Su, Y. Retrieval of diffuse attenuation coefficient in the China Seas from surface reflectance. *Opt. Express* **2013**, *21*, 15287–15297. [[CrossRef](#)] [[PubMed](#)]
25. Song, K.; Ma, J.; Wen, Z.; Fang, C.; Shang, Y.; Zhao, Y.; Wang, M.; Du, J. Remote estimation of  $K_d$  (PAR) using MODIS and Landsat imagery for turbid inland waters in Northeast China. *ISPRS J. Photogramm. Remote Sens.* **2017**, *123*, 159–172. [[CrossRef](#)]
26. Chen, J.; Cui, T.; Ishizaka, J.; Lin, C. A neural network model for remote sensing of diffuse attenuation coefficient in global oceanic and coastal waters: Exemplifying the applicability of the model to the coastal regions in Eastern China Seas. *Remote Sens. Environ.* **2014**, *148*, 168–177. [[CrossRef](#)]
27. Shi, K.; Zhang, Y.; Liu, X.; Wang, M.; Qin, B. Remote sensing of diffuse attenuation coefficient of photosynthetically active radiation in Lake Taihu using MERIS data. *Remote Sens. Environ.* **2014**, *140*, 365–377. [[CrossRef](#)]
28. Zheng, Z.; Ren, J.; Li, Y.; Huang, C.; Liu, G.; Du, C.; Lyu, H. Remote sensing of diffuse attenuation coefficient patterns from Landsat 8 OLI imagery of turbid inland waters: A case study of Dongting Lake. *Sci. Total Environ.* **2016**, *573*, 39–54. [[CrossRef](#)] [[PubMed](#)]
29. Nieke, J.; Borde, F.; Mavrocordatos, C.; Berruti, B.; Delclaud, Y.; Riti, J.B.; Garnier, T. The ocean and land colour imager (OLCI) for the Sentinel 3 GMES mission: Status and first test results. *Proc. SPIE* **2012**. [[CrossRef](#)]
30. Ma, R.; Jiang, G.; Duan, H.; Bracchini, L.; Loiselle, S. Effective upwelling irradiance depths in turbid waters: A spectral analysis of origins and fate. *Opt. Express* **2011**, *19*, 7127–7138. [[CrossRef](#)] [[PubMed](#)]
31. Duan, H.; Ma, R.; Zhang, Y.; Loiselle, S.A.; Xu, J.; Zhao, C.; Zhou, L.; Shang, L. A new three-band algorithm for estimating chlorophyll concentrations in turbid inland lakes. *Environ. Res. Lett.* **2010**, *5*, 044009. [[CrossRef](#)]
32. Luo, J.; Duan, H.; Ma, R.; Jin, X.; Li, F.; Hu, W.; Shi, K.; Huang, W. Mapping species of submerged aquatic vegetation with multi-seasonal satellite images and considering life history information. *Int. J. Appl. Earth Obs.* **2017**, *57*, 154–165. [[CrossRef](#)]
33. Ma, R.H.; Duan, H.T.; Gu, X.H.; Zhang, S.X. Detecting aquatic vegetation changes in Taihu Lake, China using multi-temporal satellite imagery. *Sensors (Basel)* **2008**, *8*, 3988–4005. [[CrossRef](#)] [[PubMed](#)]
34. Hu, C.; Lee, Z.; Ma, R.; Yu, K.; Li, D.; Shang, S. Moderate resolution imaging spectroradiometer (MODIS) observations of cyanobacteria blooms in Taihu Lake, China. *J. Geophys. Res.* **2010**, *115*. [[CrossRef](#)]
35. Duan, H.; Ma, R.; Xu, X.; Kong, F.; Zhang, S.; Kong, W.; Hao, J.; Shang, L. Two-decade reconstruction of algal blooms in China's Lake Taihu. *Environ. Sci. Technol.* **2009**, *43*, 3522–3528. [[CrossRef](#)] [[PubMed](#)]
36. Duan, H.; Feng, L.; Ma, R.; Zhang, Y.; Loiselle, S.A. Variability of particulate organic carbon in inland waters observed from MODIS Aqua imagery. *Environ. Res. Lett.* **2014**, *9*, 084011. [[CrossRef](#)]
37. Cao, Z.; Duan, H.; Feng, L.; Ma, R.; Xue, K. Climate- and human-induced changes in suspended particulate matter over Lake Hongze on short and long timescales. *Remote Sens. Environ.* **2017**, *192*, 98–113. [[CrossRef](#)]
38. Cao, Z.; Duan, H.; Shen, M.; Ma, R.; Xue, K.; Liu, D.; Xiao, Q. Using VIIRS/NPP and MODIS/Aqua data to provide a continuous record of suspended particulate matter in a highly turbid inland lake. *Int. J. Appl. Earth Obs.* **2018**, *64*, 256–265. [[CrossRef](#)]



39. Mitchell, A.B.G. Algorithms for determining the absorption coefficient for aquatic particulates using the quantitative filter technique. *Proc. SPIE* **1990**. [[CrossRef](#)]
40. Yentsch, C.S. Measurement of visible light absorption by particulate matter in the ocean. *Limnol. Oceanogr.* **1962**, *7*, 207–217. [[CrossRef](#)]
41. Bricaud, A.; Morel, A.; Prieur, L. Absorption by dissolved organic matter of the sea (yellow substance) in the uv and visible domains. *Limnol. Oceanogr.* **1981**, *26*, 43–53. [[CrossRef](#)]
42. Duan, H.; Ma, R.; Hu, C. Evaluation of remote sensing algorithms for cyanobacterial pigment retrievals during spring bloom formation in several lakes of East China. *Remote Sens. Environ.* **2012**, *126*, 126–135. [[CrossRef](#)]
43. Mueller, J.L.; Bidigare, R.R.; Trees, C.; Balch, W.M.; Dore, J.; Drapeau, D.T.; Karl, D.M.; Van Heukelem, L.; Perl, J. *Ocean Optics Protocols for Satellite Ocean Color Sensor Validation, Revision 5, Volume V: Biogeochemical and Bio-Optical Measurements and Data Analysis Protocols*; Goddard Space Flight Center: Greenbelt, MD, USA, 2003.
44. Ma, R.; Duan, H.; Lü, C.; Loiselle, S. Unusual links between inherent and apparent optical properties in shallow lakes, the case of Taihu lake. *Hydrobiologia* **2011**, *667*, 149–158. [[CrossRef](#)]
45. Vermote, E.F.; Tanre, D.; Deuze, J.L.; Herman, M.; Morcette, J.J. Second simulation of the satellite signal in the solar spectrum, 6s: An overview. *IEEE Trans. Geosci. Remote Sens.* **1997**, *35*, 675–686. [[CrossRef](#)]
46. Burns, P.; Nolin, A.W. Using atmospherically-corrected landsat imagery to measure glacier area change in the Cordillera Blanca, Peru from 1987 to 2010. *Remote Sens. Environ.* **2014**, *140*, 165–178. [[CrossRef](#)]
47. Oyama, Y.; Matsushita, B.; Fukushima, T.; Matsushige, K.; Imai, A. Application of spectral decomposition algorithm for mapping water quality in a turbid lake (lake Kasumigaura, Japan) from landsat tm data. *ISPRS J. Photogramm. Remote Sens.* **2009**, *64*, 73–85. [[CrossRef](#)]
48. Hu, C. A novel ocean color index to detect floating algae in the global oceans. *Remote Sens. Environ.* **2009**, *113*, 2118–2129. [[CrossRef](#)]
49. Wang, M.; Shi, W. Cloud masking for ocean color data processing in the coastal regions. *IEEE Trans. Geosci. Remote Sens.* **2006**, *44*, 3196–3205. [[CrossRef](#)]
50. Zhang, Y.; Ma, R.; Duan, H.; Loiselle, S.A.; Xu, J.; Ma, M. A novel algorithm to estimate algal bloom coverage to subpixel resolution in Lake Taihu. *IEEE J. Sel. Top. Appl. Earth Obs. Remote Sens.* **2014**, *7*, 3060–3068. [[CrossRef](#)]
51. Bailey, S.W.; Werdell, P.J. A multi-sensor approach for the on-orbit validation of ocean color satellite data products. *Remote Sens. Environ.* **2006**, *102*, 12–23. [[CrossRef](#)]
52. Zhang, Y.; Qin, B.; Zhu, G.; Gao, G.; Luo, L.; Chen, W. Effect of sediment resuspension on underwater light field in shallow lakes in the middle and lower reaches of the Yangtze river: A case study in Longgan lake and Taihu lake. *Sci. China* **2006**, *49*, 114–125. [[CrossRef](#)]
53. Shi, W.; Wang, M. An assessment of the black ocean pixel assumption for MODIS swir bands. *Remote Sens. Environ.* **2009**, *113*, 1587–1597. [[CrossRef](#)]
54. Stramska, M.; Stramski, D. Variability of particulate organic carbon concentration in the north polar atlantic based on ocean color observations with sea-viewing wide field-of-view sensor (seaWIFS). *J. Geophys. Res. Oceans* **2005**, *110*. [[CrossRef](#)]
55. Doxaran, D.; Lamquin, N.; Park, Y.J.; Mazeran, C.; Ryu, J.H.; Wang, M.; Poteau, A. Retrieval of the seawater reflectance for suspended solids monitoring in the east china sea using MODIS, meris and goci satellite data. *Remote Sens. Environ.* **2014**, *146*, 36–48. [[CrossRef](#)]
56. Gitelson, A.A.; Dall’Olmo, G.; Moses, W.; Rundquist, D.C.; Barrow, T.; Fisher, T.R.; Gurlin, D.; Holz, J. A simple semi-analytical model for remote estimation of chlorophyll-a in turbid waters: Validation. *Remote Sens. Environ.* **2008**, *112*, 3582–3593. [[CrossRef](#)]
57. Hou, X.; Feng, L.; Duan, H.; Chen, X.; Sun, D.; Shi, K. Fifteen-year monitoring of the turbidity dynamics in large lakes and reservoirs in the middle and lower basin of the Yangtze river, China. *Remote Sens. Environ.* **2017**, *190*, 107–121. [[CrossRef](#)]
58. Schalles, J.F.; Gitelson, A.A.; Yacobi, Y.Z.; Kroenke, A.E. Estimation of chlorophyll a from time series measurements of high spectral resolution reflectance in an eutrophic lake. *J. Phycol.* **1998**, *34*, 383–390. [[CrossRef](#)]
59. Gitelson, A. The peak near 700 nm on radiance spectra of algae and water: Relationships of its magnitude and position with chlorophyll concentration. *Int. J. Remote Sens.* **1992**, *13*, 3367–3373. [[CrossRef](#)]



60. Han, L.; Rundquist, D.C. The response of both surface reflectance and the underwater light field to various levels of suspended sediments: Preliminary results. *Photogramm. Eng. Remote Sens.* **1994**, *60*, 1463–1471.
61. Huang, C.C.; Yao, L.; Huang, T.; Zhang, M.L.; Zhu, A.X.; Yang, H. Wind and rainfall regulation of the diffuse attenuation coefficient in large, shallow lakes from long-term MODIS observations using a semi-analytical model. *J. Geophys. Res. Atmos.* **2017**. [[CrossRef](#)]
62. Lee, Z.; Carder, K.L.; Arnone, R.A. Deriving inherent optical properties from water color: A multiband quasi-analytical algorithm for optically deep waters. *Appl. Opt.* **2002**, *41*, 5755–5772. [[CrossRef](#)] [[PubMed](#)]
63. Tao, M.; Duan, H.; Cao, Z.; Loiselle, S.A.; Ma, R. A hybrid eof algorithm to improve MODIS cyanobacteria phycocyanin data quality in a highly Turbid lake: Bloom and nonbloom condition. *IEEE J. Sel. Top. Appl. Earth Obs. Remote Sens.* **2017**, *10*, 4430–4444. [[CrossRef](#)]
64. Duan, H.; Tao, M.; Loiselle, S.A.; Zhao, W.; Cao, Z.; Ma, R.; Tang, X. MODIS observations of cyanobacterial risks in a eutrophic lake: Implications for long-term safety evaluation in drinking-water source. *Water Res.* **2017**, *122*, 455–470. [[CrossRef](#)] [[PubMed](#)]
65. Liu, X.; Zhang, Y.; Wang, M.; Zhou, Y. High-frequency optical measurements in shallow Lake Taihu, China: Determining the relationships between hydrodynamic processes and inherent optical properties. *Hydrobiologia* **2014**, *724*, 187–201. [[CrossRef](#)]
66. Liang, Q.; Zhang, Y.; Ma, R.; Loiselle, S.; Li, J.; Hu, M. A MODIS-based novel method to distinguish surface cyanobacterial scums and aquatic macrophytes in Lake Taihu. *Remote Sens.* **2017**, *9*, 133. [[CrossRef](#)]
67. Qin, B.; Hu, W.; Gao, G.; Luo, L.; Zhang, J. Dynamics of sediment resuspension and the conceptual schema of nutrient release in the large shallow Lake Taihu, China. *Chin. Sci. Bull.* **2004**, *49*, 54–64. [[CrossRef](#)]
68. Li, Y.; Tang, C.; Wang, J.; Acharya, K.; Du, W.; Gao, X.; Luo, L.; Li, H.; Dai, S.; Mercy, J. Effect of wave-current interactions on sediment resuspension in large shallow Lake Taihu, China. *Environ. Sci. Pollut. Res.* **2016**, *24*, 4029–4039. [[CrossRef](#)] [[PubMed](#)]
69. Zhang, Y.; Qin, B.; Hu, W.; Wang, S.; Chen, Y.; Chen, W. Spatial-temporal variations of euphotic depth and its ecological significance of Lake Taihu. *Sci. China* **2006**, *49*, 431–442. [[CrossRef](#)]
70. Zhang, Y.; Shi, K.; Zhou, Y.; Liu, X.; Qin, B. Monitoring the river plume induced by heavy rainfall events in large, shallow, Lake Taihu using MODIS 250 m imagery. *Remote Sens. Environ.* **2016**, *173*, 109–121. [[CrossRef](#)]
71. Shi, K.; Zhang, Y.; Zhu, G.; Liu, X.; Zhou, Y.; Xu, H.; Qin, B.; Liu, G.; Li, Y. Long-term remote monitoring of total suspended matter concentration in Lake Taihu using 250m MODIS-aqua data. *Remote Sens. Environ.* **2015**, *164*, 43–56. [[CrossRef](#)]
72. Duan, H.; Ma, R.; Zhang, Y.; Loiselle, S.A. Are algal blooms occurring later in Lake Taihu? Climate local effects outcompete mitigation prevention. *J. Plankton Res.* **2014**, *36*, 866–871. [[CrossRef](#)]



© 2017 by the authors. Licensee MDPI, Basel, Switzerland. This article is an open access article distributed under the terms and conditions of the Creative Commons Attribution (CC BY) license (<http://creativecommons.org/licenses/by/4.0/>).